Phase and morphology control of hexagonal MoO_3 crystals via Na^+ interactions: A Raman spectroscopy study

C. Ingram Vargas-Consuelos[1], Marco A. Camacho-López[2], Victor H. Ramos-Sanchez[3], and Olivia A. Graeve[1,4,*]

[1] Program in Materials Science and Engineering
University of California San Diego
9500 Gilman Drive – MC 0418
La Jolla, CA 92093-0418
USA

[2] Laboratorio de Investigación y Desarrollo de Materiales Avanzados
Universidad Autónoma del Estado de México
Km 14.5 Carretera Toluca-Atlacomulco
San Cayetano de Morelos, Edo. de México, C.P. 50925
México

[3] Department of Chemistry and Biochemistry
Northern Arizona University
700 South Osborne Dr. PO Box 5698
Flagstaff, AZ 86011-5698
USA

[4] Department of Mechanical and Aerospace Engineering
University of California San Diego
9500 Gilman Drive – MC 0418
La Jolla, CA 92093-0411

* Author to whom correspondence should be addressed [Tel: +1 (858) 246-0146; ograeve@ucsd.edu; http://graeve.ucsd.edu/]

Abstract

We present the effect of sodium ions (Na^+) on the nucleation process and phase selectivity for the formation of hexagonal molybdenum trioxide crystals (*h*–MoO_3). The phase selectivity during the reaction is attributed to the interaction of Na^+ with the molecules in our precursor solution formed by metallic molybdenum dissolved in a mix of hydrochloric and nitric acids. The vibrational characteristics of the precursor solutions were studied by Raman spectroscopy in combination with density functional theory modeling, showing the presence of $[MoO_2Cl_3(H_2O)]^-$ ions within the solutions. The symmetric stretching vibration of the Mo-O bonds found at 962 cm^{-1} in $[MoO_2Cl_3(H_2O)]^-$ proved that the addition of Na^+ (in the form of dissolved NaCl) to the precursor solutions resulted only in an electrostatic interaction with the aquo (H_2O) and chloro (Cl^-) ligands in the complex. After heating the precursor solutions, X-ray diffraction, Raman spectroscopy, and scanning electron microscopy of the obtained powders showed that adding NaCl contributed to the phase selectivity of the reaction, with the Na^+ ions playing a vital role in the formation of *h*–MoO_3 over other crystalline phases. Based on the nature of the molybdenum complexes found in the precursor solutions and the structural characteristics of the powders, a formation mechanism to obtain *h*–MoO_3 is proposed. Additionally, the phase stability of the *h*–MoO_3 crystals was studied by calorimetry techniques showing that *h*–MoO_3 transforms to α–MoO_3 at ~649 K. These results provide important insights into phase control to selectively form hexagonal MoO_3.

Keywords: Hexagonal molybdenum trioxide; Raman spectroscopy; molybdenum complexed molecules.

1. Introduction

Transition metal oxides such as molybdenum trioxide (MoO_3) are of interest for their applications in diverse areas, including catalysis, the fabrication of optical and electronic devices, electrode batteries and fuel cells, color displays, smart window devices, and gas sensors.[1–6] MoO_3 is realized in three common crystalline phases, the thermodynamically stable orthorhombic phase (α–MoO_3) and two metastable phases, namely the monoclinic (β–MoO_3) and hexagonal (h–MoO_3) phases. The basic building unit of these polymorphs is the distorted MoO_6 octahedra, in which each molybdenum atom forms a bond with six oxygen atoms. In the case of α–MoO_3, the MoO_6 octahedra form a layered structure by sharing edges along the [010] direction and corners along the [001] direction, with van der Walls forces bonding the layers along the [100] direction.[6–7] In contrast, the β–MoO_3 phase has a ReO_3-type structure, in which the MoO_6 octahedral units are connected only by corner oxygen atoms to form a network.[8] The crystalline structure of interest in this work is h–MoO_3. This crystalline phase forms zigzag chains of MoO_6 octahedra in the [001] direction and links them through their *cis* positions by sharing oxygen atoms.[6,9–10] The bonding of the zigzag chains results in the formation of 1D tunnels along the [001] direction. Depending on the synthesis conditions, these tunnels may contain ammonia, water, or alkali ions,[11] resulting in unique properties and advantages compared to α–MoO_3. Although the structures of both α–MoO_3 and h–MoO_3 present a spatially open construction favorable for the insertion of atoms, the tunnel structure in h–MoO_3 increases the capacity, making the ion insertion/extraction and diffusion more favorable.[6,9] Thus, h–MoO_3 shows better performance as a cathode material for lithium and aluminum batteries[11–19] and in catalytic[20–23], photonic,[24–25] gas sensing,[26–29] photochromic and electrochromic applications.[6,30–34]

The preparation of *h*–MoO_3 powders by hydrothermal and precipitation routes is generally favored since one can achieve superior control over different reaction parameters in the precursor solutions, such as diversity of reactants, solvent media, additives, and reaction temperature.[6,11–25,28–30,32,34–41] For example, using a hydrothermal method and ammonium heptamolybdate ($(NH_4)_6Mo_7O_{24}•H_2O$) (AHM) as the precursor, Chithambararaj *et al*.[16] established a phase-selective synthesis to obtain *h*–MoO_3 instead of α–MoO_3, based on parameters such as the solvent, pH, reaction time, and temperature. The results showed that the crucial variables to obtain *h*–MoO_3 crystals were the temperature and the presence of cations such as Na^+, $Ag^{+,}$ and NH_4^+.[11,16,21,35,38] In all reported cases, the precursors used to synthesize *h*–MoO_3 are molybdenum compounds or molybdenum oxides. Thus, producing *h*–MoO_3 from a metallic molybdenum precursor is still an open question.

Here, we present a methodology to obtain *h*–MoO_3 from metallic molybdenum dissolved in a mix of hydrochloric and nitric acids and examine the structural changes of the involved reagents (*i.e.*, precursors and intermediates) using Raman spectroscopy and density functional theory modeling. We show that the effect of the addition of sodium chloride to the precursor solution is electrostatic. After heating solutions, we correlate the amount of sodium chloride added to the precursor solutions to the phase selectivity in the obtained powders. Based on the structural characterization of the powders by X-ray diffraction, Raman spectroscopy, and scanning electron microscopy, we establish the ideal amount of NaCl needed to improve the purity of the final powders and report the characteristic thermograms of the *h*–MoO_3 crystals. Lastly, a reaction scheme to obtain *h*–MoO_3 from metallic molybdenum is proposed.

2. Experimental Methodology

2.1. Preparation and characterization of precursor solutions

As a first step, a mass of 1 g of metallic molybdenum (99.95%, Alfa Aesar, Ward Hill, MA) was dissolved in 4 mL of HCl (37%, Sigma Aldrich, St. Louis, MO) and 6 mL of HNO_3 (69.3%, Fisher Scientific, Pittsburgh, PA). Subsequently, 0.05 g, 0.10 g, or 0.15 g, of NaCl (99.00%, Fisher Scientific, Pittsburgh, PA) previously dissolved in 1 mL of deionized water were added. The solution without NaCl was labeled A0, and the solutions containing NaCl were labeled A5 (0.05 g), A10 (0.10 g), and A15 (0.15 g).

Raman spectra of the four solutions were recorded on a LabRaman HR-800 (Jobin-Yvon-Horiba) system with a He-Ne laser (λ = 632.8 nm) and a 50× microscope objective lens (Olympus BX41 optical microscope). Solutions were held in a capillary tube sealed on both sides. To obtain a good signal-to-noise ratio, solutions were measured using ten 60 s exposures. We did not observe any bubbling, heating, or color changes in the solutions. All Raman measurements were recorded three times on three different independent samples to obtain the average Raman shift and the standard deviation for each band. Calibration of the Raman equipment was performed before each measurement using a silicon wafer by its characteristic Raman peak at 520 cm^{-1}.

2.2. Theoretical calculations of Raman spectra

Vibrational frequencies of $MoO_2Cl_2(H_2O)_2$, $[MoO_2Cl_4]^{2-}$, and $[MoO_2Cl_3(H_2O)]^-$, were calculated and employed to assist the Raman band assignment of the solutions. The optimized geometries and Raman vibrational modes of the putative structures of the oxo molybdenum complexes were calculated from density functional theory (DFT) with the B3LYP hybrid functional[42–43] using Orca version 4.2.3. The LAN2DZ basis set was used for all atoms in the structures,[44] as in previous related studies.[45] The effect of the solvent was treated implicitly using

the conductor-like polarizable continuum model (CPCM), where the refractive index (η) and dielectric constant (ε) used for HCl (13 M) were η = 1.425 and ε = 5.7084, respectively.[46] The final output files from the calculations, which contain the eigenvalues and eigenvectors, were processed using Chemcraft, version 1.8, to visualize the calculated Raman spectra between 200 and 1100 cm^{-1}.

2.3. Preparation and characterization of MoO_3 polymorphs

The MoO_3 powders were synthesized by heating the solutions in a Lindberg furnace at 373 K under ambient air for 12 h. After heating, white powders were recovered and labeled AP0, AP5, AP10, and AP15, corresponding to the powders produced from solutions A0 through A15. The powders were then analyzed without further washing or additional calcination treatments. The phase purity of the samples was analyzed by X-ray diffraction (XRD) on a Bruker D2 Phaser using CuKα radiation (30 kV, 10 mA). Scans were completed over the range of 10 to 60 degrees 2θ with a step size of 0.20 degrees and a dwell time of 0.3 s. Raman spectra of the resulting powders were obtained over a glass slide under conditions already reported in Section 2.1. High-resolution images of the powders were acquired on a scanning electron microscope (SEM) using an FEI Quanta 200F system operated at 12.5 kV. Thermogravimetric analysis (TGA) and differential scanning calorimetry (DSC) were performed on samples AP0 to AP15 using a Q600 thermal analyzer from TA instruments. The thermal analysis was performed under an air atmosphere at a heating rate of 10 K/min, from 323 to 773 K.

3. Results and Discussion

3.1. Raman spectroscopy of the precursor solutions

Before discussing the recorded Raman spectra of the four solutions, we briefly review the different molybdenum complexes found in hydrochloric acid solutions. Previous investigations have shown that different mono- and poly-nuclear molybdenum complexes exist in acid solutions depending on the HCl concentration.[47–56] For example, dissolving sodium molybdate $Na_2MoO_4•2H_2O$ in low HCl concentrations (≤ 2 M) produces molybdenum complexes such as $[MoO_4]^{2-}$, $[Mo_7O_{24}]^{6-}$, $[Mo_8O_{26}]^{4-}$, $[Mo_{36}O_{112}(H_2O)_{16}]^{8-}$, and $[Mo_2O_5(H_2O)_6]^{2+}$. In contrast, dissolving the same molybdate in solutions with an HCl concentration of 6 M or higher, results in the formation of chloro-complexes such as $MoO_2Cl_2(H_2O)_2$, $[MoO_2Cl_4]^{2-}$, and $[MoO_2Cl_3]^-$.[47–48,50–51,57–58] More recently, Bettinardi *et al*.[59] showed that dissolving the dichloro molybdenyl species MoO_2Cl_2 in HCl concentrations between 0.5 M and 3 M, results in predominant species of $HMoO_4^{2-}$, H_3MoO^{4+}, and H_3MoO_4Cl. Moreover, dissolving MoO_2Cl_2 in HCl concentrations between 3 M and 11 M produces MoO_2Cl_2 and $[MoO_2Cl_3]^-$ complexes. In general, regardless of the molybdenum precursor, as the HCl concentration increases, the molybdenum complexes form the molybdenyl $[MoO_2]^{2+}$ followed by chlorination. Furthermore, as the acidity of the solution increases, the relative abundance of the $[MoO_2Cl_3]^-$ complex against other species increases as well.[47,57,59]

Computationally, DFT analysis may be able to facilitate identifying the complexes present in the solutions.[45,60–61] Thus, based on previous reports and taking into consideration the preference of molybdenum to form octahedral complexes, we calculated the Raman spectra of $MoO_2Cl_2(H_2O)_2$, $[MoO_2Cl_4]^{2-}$, and $[MoO_2Cl_3(H_2O)]^-$. The identification of the molybdenum complexes was established by comparing the Raman shift of the most intense Raman peaks from the calculated and recorded Raman spectra. Our results, listed in Table 1 and illustrated in Figure 1, indicate that the calculated Raman spectrum of $[MoO_2Cl_3(H_2O)]^-$ is most comparable to the

recorded Raman spectra of the four solutions. The intensity of the calculated Raman spectrum for $[MoO_2Cl_3(H_2O)]^-$ from 200 to 450 cm^{-1} is magnified six times for visualization purposes. It shows six peaks within this region, listed in Table 1 as vibration numbers 1 to 6. Vibration 1 at 220 cm^{-1} and vibration 2 at 225 cm^{-1} correspond to the wagging and rocking modes of O-Mo-O in $[MoO_2Cl_3(H_2O)]^-$, respectively. Vibration 3 at 261 cm^{-1} corresponds to the twisting O-Mo-O mode and vibration 4 at 295 cm^{-1} corresponds to the symmetric stretching vibration of Mo-Cl. Vibration 5 at 309 cm^{-1} corresponds to the stretching of the molybdenum atom and the aqua ligand in the complex (Mo-OH_2) and vibration 6 at 357 cm^{-1} corresponds to the bending mode of O-Mo-O.

Experimentally, these six vibrations are hard to resolve because of their low Raman intensity and their low signal-to-noise ratio due to the presence of water molecules in the solutions.[61] As a result, the recorded Raman spectra only show three broad bands in the region from 200 to 450 cm^{-1}, indicated as I, II, and III in Figure 1. Band I at 244 (solution A0), 247 (solution A5), 241 (solution A10), and 240 cm^{-1} (solution A15), is formed by vibrations 1, 2, and 3. Band II at 305 (solution A0), 305 (solution A5), 295 (solution A10), and 289 cm^{-1} (solution A15), is formed by vibrations 4 and 5. Finally, band III at 385 (solution A0), 377 (solution A5), 369 (solution A10), and 370 cm^{-1} (solution A15), corresponds to the in-plane deformation of O-Mo-O within the $[MoO_2Cl_3(H_2O)]^-$ (vibration 6).

Moreover, the calculated Raman spectrum of $[MoO_2Cl_3(H_2O)]^-$ includes an asymmetric stretching vibration of Mo=O at 920 cm^{-1}, listed in Table 1 as vibration number 7. The recorded Raman spectra of the four solutions show the asymmetric vibration of Mo=O [ν_{asym}(Mo=O)] at 924 (solution A0), 917 (solution A5), 927 (solution A10), and 919 cm^{-1} (solution A15), indicated as IV in Figure 1. Adjacent to the asymmetric vibration of Mo=O, the calculated Raman spectra

includes a very intense vibration at 963 cm^{-1} corresponding to the $\nu_{sym}(Mo=O)$, listed in Table 1 as number 8. The recorded Raman spectra shows the $\nu_{sym}(Mo=O)$ vibration at 962 (solution A0), 960 (solution A5), 957 (solution A10), and 956 cm^{-1} (solution A15), indicated in Figure 1 as V. Previous reports show that the shift of the $\nu_{sym}(Mo=O)$ vibration towards lower frequencies indicates the replacement of the aquo ligands for Cl^- in molybdenum complexes.[45,47–49,51,53–55,58,61] In our case, the replacement of the aquo ligands in $[MoO_2Cl_3(H_2O)]^-$ to produce $[MoO_2Cl_4]^{2-}$ could be possible due to an increase in the concentration of Cl^- in solutions A5, A10 and A15 from the addition of NaCl.[59] In addition, our DFT calculations show that the $[MoO_2Cl_4]^{2-}$ complex presents the symmetric stretching vibration of Mo=O at 943 cm^{-1}. However, the recorded Raman spectra of solution A15 only shifts to 956 cm^{-1}. Figure 2(a) illustrates the Raman shift of the symmetric stretching vibration of Mo=O with respect to the amounts of NaCl added to the solutions. For reference, two dashed lines at 963 cm^{-1} and 943 cm^{-1} show the calculated Raman shift of the symmetric stretching vibration of Mo=O for $[MoO_2Cl_3(H_2O)]^-$ and $[MoO_2Cl_4]^{2-}$, respectively. Assuming the Raman shift will linearly decrease as the concentration of NaCl increases, it would take ~0.45 g of NaCl dissolved in 1 mL of H_2O to transition from $[MoO_2Cl_3(H_2O)]^-$ to $[MoO_2Cl_4]^{2-}$, based on the intersection of the linear fit to the experimental data [blue line in Figure 2(a)] and the calculated Raman vibration for the $[MoO_2Cl_4]^{2-}$ ion [green line in Figure 2(a)]. However, at room temperature only 1 mL of water can dissolve 0.36 g of NaCl.[46] Hence, the formation of $[MoO_2Cl_4]^{2-}$ by the addition of NaCl in this system is not possible. Therefore, we attribute the shift to lower frequencies of the $\nu_{sym}(Mo=O)$ vibration to the electrostatic interaction between the aquo ligand in $[MoO_2Cl_3(H_2O)]^-$ and the Cl^- and Na^+ ions.

Finally, the bands at 1052 (solution A0), 1051 (solution A5), 1048 (solution A10), and 1047 cm^{-1} (solution A15), correspond to the symmetric stretching vibration of N-O, referred to as ν_{sym}(N-O).[62–64] The appearance of the ν_{sym}(N-O) band at 1052 and 1051 cm^{-1} indicates the presence of HNO_3.[65] Furthermore, the shift to lower frequencies in solutions A10 to 1048 cm^{-1} and A15 to 1047 cm^{-1} indicates the de-hydrogenation of the nitrate ion due to the addition of NaCl.[65] Figure 2(b) shows the Raman shift of the N-O symmetric stretching vibration. The dashed lines at 1050 cm^{-1} and 1045 cm^{-1} indicate the Raman shift of the N-O symmetric stretching vibration for HNO_3 or NO_3^-, respectively. Similar to the Raman shift of the symmetric stretching vibration for Mo=O in Figure 2(a), we can infer that a total dissociation of the HNO_3 would occur by adding a saline solution prepared with 0.20 g of NaCl and 1 mL of H_2O in this system. This is based on the intersection of the linear fit to the experimental data [red line in Figure 2(b)] and the reported Raman vibration for the ion NO_3^- [green line in Figure 2(b)].[65]

From the above considerations, we can conclude that all solutions contain the $[MoO_2Cl_3(H_2O)]^-$ complex. Moreover, the Na^+ and Cl^- ions in the acid solutions only interact with the complexes at an electrostatic level. Thus, we propose the following reaction path for the formation of the $[MoO_2Cl_3(H_2O)]^-$ complex. First, the metallic molybdenum dissolves in the mix of HCl and HNO_3 to produce aqueous Mo^{6+} ions, while concurrently NO_3^- reduces to NO according to:[59]

$$Mo(s) + 2NO_3^-(aq) + 8H^+(aq) \longrightarrow Mo^{6+}(aq) + 2NO(g) + 4H_2O(\ell) \quad (1)$$

Subsequently, considering that the reaction occurs in a highly acidic environment in air, the presence of aqueous Mo^{6+} ions leads to the formation of the molybdenyl $[MoO_2]^{2+}$ moiety, favored by the high oxidation state of Mo. Next, similar to the formation of mercury-chlorine

complexes from an aqueous solution containing Hg^{2+} and Cl^-,[59,66] the $[MoO_2]^{2+}$ undergoes complexation by aqueous Cl^-. This reaction step is the first in a chain of three complexation reactions expressed by:[59,67–69]

$$\left[MoO_2\right]^{2+} + Cl^- \longrightarrow \left[MoO_2Cl\right]^+ \quad (2)$$

$$\left[MoO_2Cl\right]^+ + Cl^- \longrightarrow MoO_2Cl_2 \quad (3)$$

$$MoO_2Cl_2 + Cl^- \longrightarrow \left[MoO_2Cl_3\right]^- \quad (4)$$

Finally, to complete its 6-coordination sphere, $[MoO_2Cl_3]^-$ undergoes complexation by H_2O to form $[MoO_2Cl_3(H_2O)]^-$.[50,57]

3.2. Structural characterization of MoO_3 crystals

This section examines the phase formation, vibrational characteristics, and morphology of the powders obtained after heating the solutions. Figure 3(a)-(d) depicts the XRD patterns of the powders obtained after heating the four solutions. The XRD pattern of sample AP0 [Figure 3(a)] shows reflections corresponding to three different crystalline phases of molybdenum trioxide crystals. The most intense peak at 25.57° corresponds to the (120) plane of hexagonal molybdenum trioxide hydrate with the formula $MoO_3 \bullet 0.33(H_2O)$ and referred to as *h*–MoO_3 (PDF #01-078-9079). The XRD pattern also shows a reflection at 27.86° of similar intensity, corresponding to the (202) plane of orthorhombic molybdenum trioxide hydrate with the formula $MoO_3 \bullet 0.33(H_2O)$ and referred to as α–MoO_3 (PDF #01-087-1204). The XRD pattern shows three more reflections with lower intensities from the α–MoO_3 crystals at 23.00, 26.89, and 36.58°. Additionally, the XRD pattern of sample AP0 shows a reflection of medium intensity at 28.36° corresponding to the $\left(20\bar{2}\right)$ plane of monoclinic molybdenum trioxide hydrate with the

formula MoO_3•0.5(H_2O) and referred to as β–MoO_3 (PDF #01-082-1902). Moreover, five more reflections of lower intensity from the β–MoO_3 crystals are present at 24.86, 29.70, 37.34, 38.89, and 39.44°. The comparable intensities of the diffraction peaks at 25.57° (*h*–MoO_3), 27.86° (α–MoO_3), and 28.36° (β–MoO_3), suggest that the powders contain similar amounts of the three crystalline phases of MoO_3.

The XRD pattern of sample AP5 [Figure 3(b)] shows that all the reflections corresponding to *h*–MoO_3 have higher intensities compared to those of α–MoO_3, and most reflections from the β–MoO_3 crystals disappear, except for the reflection at 38.89°, corresponding to the (300) plane. Similarly, the XRD pattern of sample AP10 [Figure 3(c)] shows a considerable increase in the intensity of the reflections of the *h*–MoO_3 crystals. Furthermore, the intensity of the reflection at 27.86° from α–MoO_3 in sample AP10 decreases compared to that in sample AP5, suggesting a reduced presence of α–MoO_3. The XRD of sample AP15 shows less intense reflections from *h*–MoO_3 crystals. Additionally, there is an increase in the intensity of the peak at 23.00° from the (020) plane in α–MoO_3, indicating a greater content of orthorhombic crystals in the powder compared to sample AP10. The XRD of all powders suggest that adding NaCl to the solutions assists the nucleation process of hexagonal MoO_3. Nonetheless, sample AP15 reveals that there is a limit (0.15 g) on the amount of NaCl added to obtain more hexagonal crystals over orthorhombic MoO_3. Finally, because of the NaCl added to solutions, the powders present a reflection corresponding to the (200) plane of the cubic phase of NaCl at 31.80°. This reflection gradually intensifies as sodium chloride increases from solution A5 to A15, thus the NaCl present in solution recrystallizes at the end of the heat treatment.

Figure 3(e)-(g) illustrates the three different crystal structures of MoO_3. Figure 3(e) represents the polyhedral representation of α–MoO_3 and indicates the corner and edge sharing of the MoO_6 clusters. Figure 3(f) represents a β–MoO_3 crystal where the MoO_6 clusters only share corners. Figure 3(g) represents the *h*–MoO_3 crystal, indicating the tunnel structure and the "A" sites where ammonium ions or water molecules are stored to stabilize the structure. The presence of NH_4^+ ions or crystalline water trapped inside the tunnels comes from the decomposition of the reagents used to prepare *h*–MoO_3. For example, using ammonium heptamolybdate [$(NH_4)_6Mo_7O_{24}•H_2O$] as the precursor, one can obtain *h*–MoO_3 containing NH_4^+ ions that stabilize the hexagonal structure. Starting from sodium molybdate [Na_2MoO_4] or molybdic acid, the resulting *h*–MoO_3 contains water molecules to stabilize the hexagonal tunnels.[15–17,70] As the NH_4^+ is not part of the crystalline structure of *h*–MoO_3 it typically requires thermogravimetric measurements to determine its presence.[16,21,28,35,39]

3.3. Vibrational analysis of MoO_3 crystals

The vibrational characteristics of the powders were analyzed by Raman spectroscopy. The standard group theory analysis of *h*–MoO_3 leads to 69 optical modes and three acoustic modes at the Brillouin zone, and the irreducible representation of the optical modes of the group C_{6h} can be described by:[71]

$$\Gamma = 8A_g + 3A_u + 4B_g + 8B_u + 8E_{2g} + 4E_{2u} + 4E_{1g} + 7E_{1u*} \quad (5)$$

Selection rules predict only twenty Raman active modes belonging to the A_g, E_{2g}, and E_{1g} irreducible representations from these modes. Typically, the recorded Raman spectra show fewer Raman vibrations than those predicted by group theory, since factor group splitting for most modes is not resolved in the unpolarized spectrum.[71–72] Most studies[12,20,37–38] have observed

between nine and eleven Raman vibrations, except Moura *et al*.,[71] who observed eighteen. Table 2 summarizes the Raman vibrations found in previous studies.

Figure 4(a)-(d) illustrates the Raman spectra of samples AP0 to AP15. The Raman vibrations are enumerated from number 1 to 19 and summarized in Table 3. The vibration assignments for *h*–MoO_3 are based on the vibrational modes calculated by Moura *et al*.[71] using DFPT and early experimental results.[12,20,37–38] For the case of α–MoO_3 and β–MoO_3, we assigned the Raman vibrations based on previous experimental reports.[37,73–77] Note that almost all bands in the region of the Raman spectra from 220 cm^{-1} to 650 cm^{-1} belong to different librational modes of O-Mo-O [scissoring (sc), twisting (tw), and rotational (ρ)] in *h*–MoO_3, except for Raman vibrations 3, 4 and 8, which belong to α–MoO_3.

The very weak vibration at 264 cm^{-1} (vibration 3) in sample AP0 belongs to the scissoring vibration of O-Mo-O in α–MoO_3 and is only observed in this sample.[7] Vibration 4 at 283 (sample AP0), 280 (sample AP5), and 276 cm^{-1} (sample AP15), belong to the wagging vibration in the O-Mo-O bonds of α–MoO_3 crystals.[73,76] Note that vibration 4 decreases in intensity from sample AP0 to sample AP5 and is not present in sample AP10. At the same time, vibration 2 first appears in sample AP5 and increases in intensity in sample AP10 at 257 and 253 cm^{-1}, respectively. Moura *et al*.[71] showed that vibration 2 is the second most intense in the Raman spectrum of *h*–MoO_3, belonging to the twisting vibration of the O-Mo-O bonds. Therefore, the intensity changes observed in vibrations 4 and 2 suggest that the presence of NaCl during the thermal treatment helps in the nucleation and growth of *h*–MoO_3 over α–MoO_3. Furthermore, vibration 4 appears again in sample AP15 at 276 cm^{-1}, whereas vibration 2 at 253 cm^{-1} is barely noticeable. This change indicates that 0.15 g of NaCl exceeds the amount needed to improve the formation of *h*–MoO_3 crystals over α–MoO_3, which agrees with our XRD

findings. Furthermore, samples AP0 and AP15 show a small shoulder indicated as vibration 8 at 476 cm^{-1}. This vibration belongs to the stretching modes of the O-Mo-O bonds in α–MoO_3.[73]

The spectral regions from 650 to 750 cm^{-1} in samples AP0, AP5, and AP15, show two Raman vibrations close to each other, labeled 10 and 11. Previous DFPT analysis and recorded Raman spectra of anhydrous *h*–MoO_3 only shows one Raman vibration within this region at 702 and 690 cm^{-1}, respectively, belonging to the scissoring vibration in the direction of the *z*-axis of the O-Mo-O bonds.[71] However, earlier studies showed that the splitting of the Raman band between 650 and 750 cm^{-1} is related to the hydration of different polymorphs of MoO_3.[76] Thus, according to the results in Figure 4, samples AP0, AP5, and AP15, are hydrate forms of MoO_3. Indeed, the XRD of samples AP0, AP5, and AP15, show the presence of α–MoO_3, β–MoO_3, and *h*–MoO_3 as hydrated oxides. Therefore, the splitting of this Raman vibration is expected. Although the XRD of all samples showed the presence of hydrated oxide phases, the Raman spectrum of sample AP10 only shows a single Raman vibration at 695 cm^{-1}. In principle, the high crystallinity and relatively high purity of sample AP10, compared to samples AP0, AP5, and AP15, as shown by XRD, produces such intense Raman vibrations that the water present in the sample cannot be detected. Most Raman vibrations from 750 to 1100 cm^{-1} belong to stretching vibrations of the Mo=O double bond in *h*–MoO_3, except vibration 12, which belongs to the stretching vibration of the Mo=O bonds in α–MoO_3.[71] This Raman vibration is present in samples AP0, AP5, and AP10 at 829, 825, and 836 cm^{-1}, respectively. All samples exhibit a different number of Raman bands within the 750-1100 cm^{-1} region, related to minor defects in the *h*–MoO_3 crystals.[71]

Even though XRD showed the presence of β–MoO_3 crystals in all samples, Raman spectroscopy cannot record specific bands for that crystal structure. However, some reports show

that vibration 7 found at 416 (sample AP0), 415 (sample AP5), 417 (sample AP10), and 413 cm^{-1} (sample AP15), is present in *h*–MoO_3 and β–MoO_3.[12,37,71,75–77] In *h*–MoO_3, vibration 7 corresponds to the scissoring vibration of the O-Mo-O bonds.[71] To our knowledge, there is no formal assignment of this Raman vibration to β–MoO_3 crystals, and it is only referred to as the bending vibration of the O-Mo-O bonds.[75–77] Additionally, vibration 14 present in samples AP5 and AP10 is reported for *h*–MoO_3 and β–MoO_3 as a stretching vibration of the Mo=O bonds.[12,20,37,71,75–76] Although the β–MoO_3 phase presents several other Raman vibrations in the 200-1100 cm^{-1} spectral region, the similarities in the bonding of the structural units in both crystals (β–MoO_3 and *h*–MoO_3) produce Raman vibrations with very close wavenumbers. Therefore, the simultaneous detection of β–MoO_3 and *h*–MoO_3 using Raman spectroscopy is not trivial.

Figure 5(a)-(d) illustrates the scanning electron micrographs obtained from sample AP0. We find the presence of hexagonal bars, needle-like structures, rectangular bars made from thin needles, and spherical particles. The hexagonal bars belong to *h*–MoO_3 crystals.[12,22,35] The needle-like structures and the rectangular bars made from thin needles agree with previous findings showing that orthorhombic crystals of α–MoO_3 grow into elongated structures.[7,74,78] Furthermore, recent studies show that α–MoO_3 can also grow in the form of spheres.[79] Hence, it is likely that the spheres in Figure 5(d) belong α–MoO_3 crystals. The micrographs in Figure 5(e)-(h) correspond to sample AP5. The XRD pattern and Raman spectra of this sample show the presence of *h*–MoO_3, β–MoO_3, and α–MoO_3, although the sample shows majority *h*–MoO_3. Thus, the SEM micrographs only show hexagonal bars and hexagonal plates, usually found only in *h*–MoO_3.[6,12,16,20] The micrographs of sample AP10 in Figure 5(i)-(l) show hexagonal bars, hollow hexagonal bars corresponding to *h*–MoO_3, and darker regions [Figure 5(k)]. For sample

AP15 in Figure 5(m)-(p), we see hexagonal crystals, broken irregular bars, hollow hexagonal bars, needle-like structures, and darker rectangular structures [Figure 5(p)]. The presence of needle-like structures and incomplete elongated crystals show the presence of α–MoO_3, which agrees with the XRD and Raman results. Thus, from SEM it is seen that powder morphologies[80–85] can be controlled by varying the phases in this material. The darker rectangular structures from samples AP10 and AP15 were analyzed by EDS and are depicted in Figure 6. The EDS results reveal the presence of molybdenum, nitrogen, oxygen, sodium, and silicon. The molybdenum and oxygen signals belong to the MoO_3, and the silicon is from the substrate used to image the powders. The nitrogen signal could be attributed to remnant HNO_3 at the end of the heat treatment. In both samples, we attribute the sodium signal to the NaCl recrystallized at the end of the synthesis, as previously shown by XRD.

3.4. Proposed growth model of *h*–MoO_3

Based on the experimental and computational results, we now describe the phase formation mechanism of *h*–MoO_3 and the other MoO_3 polymorphs starting from metallic molybdenum. Previously, Zheng *et al*.[6] proposed a reaction approach to describe the formation of α–MoO_3 and *h*–MoO_3 from the peroxomolybdate species $MoO_4(H_2O)$. Their approach shows that during a heat treatment, the peroxomolybdate undergoes a series of dehydration and deoxidation steps to form MoO_6 as the building units of the MoO_3 crystals. Zheng *et al*.[6] demonstrated that adding $NaNO_3$ to the synthesis contributed to the formation of *h*–MoO_3 over α–MoO_3. Preference for the formation of *h*–MoO_3 suggests that the presence of Na^+ ions changes the oxolation mode of the building units, allowing the MoO_6 octahedra to share two vertexes at the ortho-position. Thus, zigzag chains interlink each other through the *cis* position,

leading to the spontaneous arrangement of hexagonal MoO_3 with one-dimensional tunnel structures along the *z*-axis.

Similarly, we propose that during the thermal treatment of solutions A0 to A15, the dechlorination and dehydration of the $[MoO_2Cl_3(H_2O)]^-$ produce MoO_6 building units that further condense in edge-sharing or corner-sharing arrangements to then form crystalline MoO_3. The fact that the XRD of sample A0 [Figure 3(a)] shows three different crystalline phases of MoO_3 at the end of the heat treatment suggests at least three possible reaction paths [see Figure 7]. Although the conditions to obtain edge-sharing or corner-sharing arrangements remain unclear, it is well known that β–MoO_3 crystals are formed by corner-sharing MoO_6 units, while edge-sharing MoO_6 units are the principal constituent of α–MoO_3 and *h*–MoO_3.[8–9,30,86] Therefore, the formation of edge-sharing *vs* corner-sharing arrangements during the synthesis is essential for obtaining α–MoO_3 and *h*–MoO_3 or β–MoO_3 crystals, respectively. Moreover, the presence of NO_3^- ions has been related to the formation of β–MoO_3.[87] Thus, we propose that the formation of corner-sharing octahedral arrangements is related to the interaction of NO_3^- ions from the HNO_3 in solution with some of the $[MoO_2Cl_3(H_2O)]^-$ complexes. Hence, the complexes that lack interaction with the NO_3^- ions form edge-sharing MoO_6.

Next, the corner-sharing octahedral arrangements are joined by oxygen corner atoms to form a network and grow β–MoO_3. On the other hand, we propose that the edge-sharing MoO_6 structures undergo two different routes to form α–MoO_3 or *h*–MoO_3. The formation of α–MoO_3 starts with the edge-sharing structures condensing with other units sharing edges along the [010] direction and corners along with the [001] direction to form zigzag chains and layers, respectively. At the same time, van der Walls forces hold the layers along the [100] direction, as

was reported before.[7] Moreover, those MoO_6 structures that become oriented by the positive charges during the synthesis (H^+), condense into zigzag chains of MoO_6 octahedra in the [001] direction linking them through their *cis* position by sharing oxygen atoms to form one-dimensional tunnel structures, characteristic of *h*–MoO_3. When NaCl is used as a mineralizer, Na^+ cations dissociate as hydrated ions in aqueous solution, which act as bond bridges between the growth units to form crystal nuclei.[77,88] In our case, and as shown in previous reports, the hydrated Na^+ forms bond bridges between MoO_6 units to form the crystal nucleus, stabilizing the hexagonal tunnels during the initial stage to form *h*–MoO_3.[6,89] During the thermal process, the Na^+ is stripped away from the hexagonal tunnels via repeated water wash to then recrystallize into NaCl.

3.5. Thermal analysis

The phase stability of the powder samples at temperatures ranging from 323 to 773 K is described in Figure 8 (samples AP0 and AP5) and Figure 9 (samples AP10 and AP15). From thermogravimetric analyses, we obtained the weight loss percentage due to the removal of water and nitrate products from the surface and the tunnels of the MoO_3 crystals. The thermogravimetric analyses (TGA) data was differentiated with respect to time and used to identify the temperature at which different compounds are removed from the samples, marked as DTG in the figure (blue curve). Table 4 summarizes our findings. Below 423 K, the DTG results indicate no weight loss on sample AP0. The DTG results of samples AP5, AP10, and AP15 show a weight loss at 398 K, 393 K, and 393 K respectively. This weight loss can be related to the desorption of physically absorbed water on the surface of *h*–MoO_3 crystals.[35] It is known that α–MoO_3 crystals show no significant mass losses during heat treatments.[16,21,39] Thus, the fact that sample AP0 shows no weight loss below 423 K might be related to the higher content of

α–MoO_3 crystals present in the powder, as shown by XRD. It is known that after the synthesis of *h*–MoO_3, nitrates and other by-products remain on the surface of the crystals.[35,40] Considering that our synthetic approach includes HNO_3 and HCl, a remnant of hydrochloric acid and nitrate products in the samples is expected. According to previous DTG results, the nitrate and hydrochloric acid by-products are eliminated between 473-523 K and 523-533 K, respectively.[16,90] Therefore, the weight losses identified by DTG at 503 K and 550 K (sample AP0), 488 K and 536 K (sample AP5), 494 K and 531 K (sample AP10), and 493 K and 541 K (sample AP15), correspond to the elimination of nitrates and HCl physically adsorbed on the surface of the powders. Our findings agree with those from Chithambararaj *et al*.,[16,28,35] showing that the water and nitrate molecules on the surfaces of *h*–MoO_3 crystals evaporate around 398 K and around 523 K, respectively. Furthermore, the endothermic peaks from the DSC corroborate with the evaporation temperature of these species.

Previous studies using ammonium heptamolybdate as a precursor to prepare *h*–MoO_3 showed that the two peaks in the 663-683 K region of the DTG correspond to weight loss due to the release of ammonia and water contained inside the tunnel structure of *h*–MoO_3, followed by the phase transformation from *h*–MoO_3 to α–MoO_3 at around 686 K.[16] Since our synthesis approach is free of ammonia precursors, we would only expect to observe a single peak in the DTG corresponding to the release of crystalline water at ~683 K. The DTG in sample AP0 shows no changes that suggest the release of water residing within the crystal. However, from the DSC we can observe two exothermic peaks at 663 K and 706 K, indicating the phase transformation of β–MoO_3 and *h*–MoO_3 into α–MoO_3 [see Figure 8(a)], respectively.[16,87] On the other hand, the DTG of samples AP5, AP10, and AP15 show a weight loss at 643 K, 646 K, and 647 K, indicating the loss of crystalline water from the hexagonal tunnels in *h*–MoO_3 [see Figure

8(b) and Figure 9(a)-(b), blue lines]. This is followed by an exothermic peak in the DSC located at 648 K, 649 K, and 650 K, indicating the phase transformation of *h*–MoO_3 to α–MoO_3 [see Figure 8(b) and Figure 9(a)-(b), red lines]. Although the XRD results show that samples AP10 and AP15 contain β–MoO_3, the minimal amount present in each sample makes the detection of the phase change from β–MoO_3 to α–MoO_3 difficult by DSC. The total weight loss according to TGA was 6% (sample AP0), 6.5% (sample AP5), 5.2% (sample AP10), and 6.1% (sample AP15) [see Figure 8(a)-(b) and Figure 9(a)-(b), green lines], which agrees with previous reports on samples containing *h*–MoO_3 and heat treated from 323 K to 773 K.[16,28,35]

In summary, we present a detailed analysis of the formation of *h*–MoO_3 crystals from metallic molybdenum, the precursor solution vibrational characteristics, and the influence of NaCl in the phase selectivity of the reaction. We have determined that the sodium ions interact electrostatically with the species in the precursor solutions and help orient the building units to form *h*–MoO_3 during the thermal treatment. XRD shows that the NaCl is recrystallized at the end of the heat treatment. Moreover, the thermal analysis of *h*–MoO_3 crystals shows that water molecules are contained inside the tunnel structure of *h*–MoO_3, helping to stabilize the structure. Thus, this study provides a new approach to obtaining metastable *h*–MoO_3.

4. Conclusions

In this study, a detailed Raman analysis of a solution containing metallic molybdenum dissolved in a mix of HCl and HNO_3 showed the presence of $[MoO_2Cl_3(H_2O)]^-$. This was determined with the help of density functional theory modeling by calculating the Raman spectra of different possible molecules present in the solution. The Raman spectra showed that by adding different amounts of NaCl to the solution, the symmetric stretching vibration of Mo=O shifted

from 962 cm^{-1} to 956 cm^{-1}. This shift was attributed to electrostatic interactions of the $[MoO_2Cl_3(H_2O)]^-$ molecules with the Na^+ ions in the solution. X-ray diffraction of powder samples obtained after heating the solutions without NaCl revealed the formation of α–MoO_3, β–MoO_3, and *h*–MoO_3 crystals. In the case of the powder samples obtained from heating solutions containing NaCl, the diffraction patterns showed that *h*–MoO_3 was the major crystalline phase in the powders. Additionally, the diffraction patterns revealed that the NaCl recrystallized at the end of the heat treatment, indicating that the NaCl only acted as a mineralizer during the synthesis of MoO_3 powders and contributed to the phase selectivity of the reaction to generate *h*–MoO_3. Raman spectroscopy of the powders revealed the presence of α–MoO_3 and *h*–MoO_3. However, the similarity in the Raman shift of the bands in β–MoO_3 and *h*–MoO_3 crystals hindered the identification of β–MoO_3.

The phase selectivity of the reaction to generate *h*–MoO_3 in the presence of NaCl was attributed to the interaction between the $[MoO_2Cl_3(H_2O)]^-$ molecules with the Na^+ ions during the heat treatment. This interaction was proposed to influence the dichlorination, condensation and further dehydration process of the $[MoO_2Cl_3(H_2O)]^-$ molecules to form *h*–MoO_3 crystals. Thermal analysis of the powders revealed that *h*–MoO_3 contains water molecules to help stabilize the crystal, most likely within the tunnels of the structure. Once the water molecules were removed, the phase transformation from *h*–MoO_3 to α–MoO_3 occurred at ~650 K. These findings result in a methodology to obtain *h*–MoO_3 starting from metallic molybdenum, using NaCl to control the nucleation and growth of the crystals. Compared to α–MoO_3 and β–MoO_3, the tunnels present in the *h*–MoO_3 crystals might enhance the ionic conductivity of molybdenum trioxide, useful for applications in supercapacitors, batteries, and photochromic devices.

5. Acknowledgments

This project was funded by the National Science Foundation (grant #2016247).

6. References

(1) Zhu, Y.; Yao, Y.; Luo, Z.; Pan, C.; Yang, J.; Fang, Y.; Deng, H.; Liu, C.; Tan, Q.; Liu, F.; et al. Nanostructured MoO_3 for efficient energy and environmental catalysis. *Molecules* **2019**, *25* (1), 18.

(2) Wang, J.; Zhou, Q.; Peng, S.; Xu, L.; Zeng, W. Volatile organic compounds gas sensors based on molybdenum oxides: A mini review. *Front. Chem.* **2020**, *8*, 339.

(3) Gong, Y.; Dong, Y.; Zhao, B.; Yu, R.; Hu, S.; Tan, Z. Diverse applications of MoO_3 for high performance organic photovoltaics: Fundamentals, processes and optimization strategies. *J. Mater. Chem. A* **2020**, *8* (3), 978–1009.

(4) Malik R.; Joshi N.; Tomer V. K.; Advances in the designs and mechanisms of MoO_3 nanostructures for gas sensors: a holistic review. *Mater. Adv.* **2021**, *2* (13), 4190–4227.

(5) He, T.; Yao, J. Photochromism of molybdenum oxide. *J. Photochem. Photobiol. C Photochem. Rev.* **2003**, *4* (2), 125–143.

(6) Zheng, L.; Xu, Y.; Jin, D.; Xie, Y. Novel metastable hexagonal MoO_3 nanobelts: Synthesis, photochromic, and electrochromic properties. *Chem. Mater.* **2009**, *21* (23), 5681–5690.

(7) Py, M. A.; Maschke, K. Intra- and interlayer contributions to the lattice vibrations in MoO_3. *Phys. B+C* **1981**, *105* (1–3), 370–374.

(8) Parise, J. B.; McCarron III, E. M.; Von Dreele, R.; Goldstone, J. A. β-MoO_3 produced from a novel freeze drying route. *J. Solid State Chem.* **1991**, *93* (1), 193–201.

(9) Zhao, J.; Ma, P.; Wang, J.; Niu, J. Synthesis and structural characterization of a novel three-dimensional molybdenum-oxygen framework constructed from Mo_3O_9 units. *Chem. Lett.* **2009**, *38* (7), 694–695.

(10) McCarron III, E. M.; Thomas, D. M.; Calabrese, J. C. Hexagonal molybdates: Crystal Structure of $(Na{\cdot}2H_2O)Mo_{5.33}[H_{4.5}]_{0.67}O_{18}$. *Inorg. Chem.* **1987**, 26 (3), 370-373.

(11) Guo, J.; Zavalij, P.; Whittingham, M. S. Metastable hexagonal molybdates: Hydrothermal preparation, structure, and reactivity. *J. Solid State Chem.* **1995**, *117* (2), 323–332.

(12) Lunk, H. -J.; Hartl, H.; Hartl, M. A.; Fait, M. J. G.; Shenderovich, I. G.; Feist, M.; Frisk, T. A.; Daemen, L. L. Mauder, D.; Eckelt, R.; et al. "Hexagonal molybdenum trioxide" - Known for 100 years and still a fount of new discoveries. *Inorg. Chem*. **2010**, *49* (20), 9400–9408.

(13) Tang, Q.; Wang, L.; Zhu, K.; Shan, Z.; Qin, X. Synthesis and electrochemical properties of H-MoO_3/graphene composite. *Mater. Lett*. **2013**, 100, 127–129.

(14) Kumar, V.; Wang, X.; Lee, P. S. Synthesis of pyramidal and prismatic hexagonal MoO_3 nanorods using thiourea. *CrystEngComm*. **2013**, *15* (38), 7663–7669.

(15) Xu, Y.; Xie, L.; Zhang, Y.; Cao, X. Hydrothermal synthesis of hexagonal MoO_3 and its reversible electrochemical behavior as a cathode for Li-ion batteries. *Electron. Mater. Lett*. **2013**, *9* (5), 693–696.

(16) Chithambararaj, A.; Rajeswari Yogamalar, N.; Bose, A. C. Hydrothermally synthesized h-MoO_3 and α-MoO_3 nanocrystals: New findings on crystal-structure-dependent charge transport. *Cryst. Growth Des*. **2016**, *16* (4), 1984–1995.

(17) Song, J.; Wang, X.; Ni, X.; Zheng, H.; Zhang, Z.; Ji, M.; Shen, T.; Wang, X. Preparation of hexagonal-MoO_3 and electrochemical properties of lithium intercalation into the oxide. *Mater. Res. Bull*. **2005**, *40* (10), 1751–1756.

(18) Joseph, J.; O'Mullane, A. P.; Ostrikov, K. Hexagonal molybdenum trioxide (h-MoO_3) as an electrode material for rechargeable aqueous aluminum-ion batteries. *ChemElectroChem* **2019**, *6* (24), 6002–6008.

(19) Kumar, V.; Lee, P. S. Redox active polyaniline-h-MoO_3 hollow nanorods for improved pseudocapacitive performance. *J. Phys. Chem. C* **2015**, *119* (17), 9041–9049.

(20) Pan, W.; Tian, R.; Jin, H.; Guo, Y.; Zhang, L.; Wu, X.; Zhang, L.; Han, Z.; Liu, G.; Li, J.; et al. Structure, optical, and catalytic properties of novel hexagonal metastable *h*-MoO_3 nano- and microrods synthesized with modified liquid-phase processes. *Chem. Mater*. **2010**, *22* (22), 6202–6208.

(21) Chithambararaj, A.; Sanjini, N. S.; Velmathi, S.; Chandra Bose, A. Preparation of h-MoO_3 and α-MoO_3 nanocrystals: Comparative study on photocatalytic degradation of methylene blue under visible light irradiation. *Phys. Chem. Chem. Phys*. **2013**, *15* (35), 14761–14769.

(22) Wongkrua, P.; Thongtem, T.; Thongtem, S. Synthesis of h- and α-MoO_3 by refluxing and calcination combination: Phase and morphology transformation, photocatalysis, and photosensitization. *J. Nanomater*. **2013**, *2013*, 702679.

(23) Manivel, A.; Lee, G. -J.; Chen, C. -Y.; Chen, J. -H.; Ma, S. -H.; Horng, T. -L.; Wu, J. J. Synthesis of MoO_3 nanoparticles for azo dye degradation by catalytic ozonation. *Mater. Res. Bull*. **2015**, *62*, 184–191.

(24) Song, J.; Ni, X.; Zhang, D.; Zheng, H. Fabrication and photoluminescence properties of hexagonal MoO_3 rods. *Solid State Sci*. **2006**, *8* (10), 1164–1167.

(25) Guan, Z. S.; Zhang, Y.; Zhang, Q.; Li, D. X. Controllable size, shape and morphology of molybdic acid self-aggregated with rhodamine B to construct functional material. *J. Colloid Interface Sci*. **2006**, *302* (1), 113–122.

(26) Chu, X.; Liang, S.; Sun, W.; Zhang, W.; Chen, T.; Zhang, Q. Trimethylamine sensing properties of sensors based on MoO_3 microrods. *Sensors Actuators, B Chem*. **2010**, *148* (2), 399–403.

(27) Bai, S.; Chen, S.; Chen, L.; Zhang, K.; Luo, R.; Li, D.; Liu, C. C. Ultrasonic synthesis of MoO_3 nanorods and their gas sensing properties. *Sensors Actuators, B Chem*. **2012**, 174 (2), 51–58.

(28) Chithambararaj, A.; Bose, A. C. Investigation on structural, thermal, optical and sensing properties of meta-stable hexagonal MoO_3 nanocrystals of one dimensional structure. *Beilstein J. Nanotechnol*. **2011**, *2* (1), 585–592.

(29) Liu, Y.; Yang, S.; Lu, Y.; Podval'naya, N. V.; Chen, W.; Zakharova, G. S. Hydrothermal synthesis of *h*-MoO_3 microrods and their gas sensing properties to ethanol. *Appl. Surf. Sci.* **2015**, *359*, 114–119.

(30) Song, Y.; Zhao, Y.; Huang, Z.; Zhao, J. Aqueous synthesis of molybdenum trioxide (*h*-MoO_3, α-$MoO_3 \cdot H_2O$ and *h*-/α-MoO_3 composites) and their photochromic properties study. *J. Alloys Compounds* **2017**, *693*, 1290–1296.

(31) Deki, S.; Béléké, A. B.; Kotani, Y.; Mizuhata, M. Liquid phase deposition synthesis of hexagonal molybdenum trioxide thin films. *J. Solid State Chem*. **2009**, *182* (9), 2362–2367.

(32) Shen, Y.; Huang, R.; Cao, Y.; Wang, P. Synthesis and photochromic properties of formaldehyde-induced MoO_3 powder. *Mater. Sci. Eng. B* **2010**, *172* (3), 237–241.

(33) Song, J.; Li, Y.; Zhu, X.; Zhao, S.; Hu, Y.; Hu, G. Preparation and optical properties of hexagonal and orthorhombic molybdenum trioxide thin films. *Mater. Lett*. **2013**, *95*, 190–192.

(34) Jittiarporn, P.; Sikong, L.; Kooptarnond, K.; Taweepreda, W. Effects of precipitation temperature on the photochromic properties of h-MoO_3. *Ceram. Int.* **2014**, *40* (8), 13487–13495.

(35) Chithambararaj, A.; Chandra Bose, A. Role of synthesis variables on controlled nucleation and growth of hexagonal molybdenum oxide nanocrystals: Investigation on thermal and optical properties. *CrystEngComm* **2014**, 16 (27), 6175–6186.

(36) Sotani, N. Studies on the hexagonal hydrate of molybdenum trioxide. The physical properties of the hydrate and its changes on heat treatments in air, in hydrogen, and in a hydrogen–Thiophene mixture. *Bull. Chem. Soc. Jpn.* **1975**, *48* (6), 1820–1825.

(37) Silveira, J. V.; Batista, J. A.; Saraiva, G. D.; Mendes Filho, J.; Souza Filho, A. G.; Hu, S.; Wang, X. Temperature dependent behavior of single walled MoO_3 nanotubes: A Raman spectroscopy study. *Vib. Spectrosc*. **2010**, *54* (2), 179–183.

(38) Atuchin, V. V.; Gavrilova, T. A.; Kostrovsky, V. G.; Pokrovsky, L. D.; Troitskaia, I. B. Morphology and structure of hexagonal MoO_3 nanorods. *Inorg. Mater*. **2008**, *44* (6), 622–627.

(39) Chithambararaj, A.; Chandra Bose, A. Hydrothermal synthesis of hexagonal and orthorhombic MoO_3 nanoparticles. *J. Alloys Compd*. **2011**, *509* (31), 8105–8110.

(40) Ramana, C. V.; Atuchin, V. V.; Troitskaia, I. B.; Gromilov, S. A.; Kostrovsky, V. G.; Saupe, G. B. Low-temperature synthesis of morphology controlled metastable hexagonal molybdenum trioxide (MoO_3). *Solid State Commun*. **2009**, *149* (1–2), 6–9.

(41) Kumar, V.; Sumboja, A.; Wang, J.; Bhavanasi, V.; Nguyen, V. C.; Lee, P. S. Topotactic phase transformation of hexagonal MoO_3 to layered MoO_3-II and its two-dimensional (2D) nanosheets. *Chem. Mater.* **2014**, *26* (19), 5533–5539.

(42) Becke, A. D. Density-functional thermochemistry. III. The role of exact exchange. *J. Chem. Phys.* **1993**, *98* (7), 5648–5652.

(43) Lee, C.; Yang, W.; Parr, R. G. Development of the Colle-Salvetti correlation-energy formula into a functional of the electron density. *Phys. Rev. B* **1988**, *37* (2), 785–789.

(44) Hay, P. J.; Wadt, W. R. *Ab initio* effective core potentials for molecular calculations. Potentials for the transition metal atoms Sc to Hg. *J. Chem. Phys*. **1985**, *82* (1), 270–283.

(45) Jalilehvand, F.; Mah, V.; Leung, B. O.; Ross, D.; Parvez, M.; Aroca, R. F. Structural characterization of molybdenum(V) species in aqueous HCl solutions. *Inorg. Chem.* **2007**, *46* (11), 4430–4445.

(46) Lide, D. R. CRC Handbook of Chemistry and Physics, 90th ed.; Taylor & Francis, **2009**.

(47) Coddington, J. M.; Taylor, M. J. Molybdenum-95 nuclear magnetic resonance and vibrational spectroscopic studies of molybdenum (VI) species in aqueous solutions and solvent extracts from hydrochloric and hydrobromic acid: Evidence for the complexes $[Mo_2O_5(H_2O)_6]^{2+}$, $[MoO_2X_2(H_2O)_2]$ (X = Cl or Br), and $[MoO_2Cl_4]^{2-}$. *J. Chem. Soc., Dalton Trans.* **1990**, (1), 41–47.

(48) Griffith, W. P.; Wickins, T. D. Raman studies on species in aqueous solutions. Part II. Oxy-species of metals of groups VIA, VA, and IVA. *J. Chem. Soc. A* **1967**, (0), 675–679.

(49) Griffith, W. P.; Lesniak, P. J. B. Raman studies on species in aqueous solutions. Part III. Vanadates, molybdates, and tungstates. *J. Chem. Soc. A* **1969**, (0), 1066–1071.

(50) Stiefel, E. I. The coordination and bioinorganic chemistry of molybdenum, *Progr. Inorg. Chem.* **2007**, *22*, 1–223.

(51) Taylor, M. J.; Rickard, C. E. F.; Kloo, L. A. Vibrational and crystallographic studies of dioxohalogenomolybdenum(VI) complexes with crown ethers. *J. Chem. Soc., Dalton Trans.* **1998**, (19), 3195–3198.

(52) Arnaiz, F. J.; Aguado, R.; Sanz-Aparicio, J.; Martinez-Ripoll, M. Addition compounds of dichlorodioxomolybdenum (VI) from hydrochloric acid solutions of molybdenum trioxide. Crystal structure of dichlorodioxodiaquamolybdenum(VI) bis(2,5,8-trioxanonane). *Polyhedron* **1994**, *13* (19), 2745–2749.

(53) Himeno, S.; Hasegawa, M.; Saito, A. On molybdenum(IV) and molybdenum(III) species in HCl solutions. *Inorganica Chim. Acta* **1985**, *101* (2), L15–L17.

(54) Himeno, S.; Hasegawa, M. Spectrophotometric studies on the monomer-monomer equilibration of Mo(VI) in hydrochloric acid solutions. *Inorganica Chim. Acta* **1983**, *73*, 255–259.

(55) Himeno, S.; Hasegawa, M. Raman studies on molybdenum(V) species in HCl solutions. *Inorganica Chim. Acta* **1984**, *83* (1), L17–L18.

(56) Sadayuki, H.; Hirotaka, N.; Tadaharu, U. Raman studies on the identification of isopolymolybdates in aqueous solution. *Bull. Chem. Soc. Jpn.* **1997**, *70* (3), 631–637.

(57) Tkac, P.; Paulenova, A. Speciation of molybdenum (VI) in aqueous and organic phases of selected extraction systems. *Separ. Sci. Tech*. **2008**, *43* (9–10), 2641–2657.

(58) Taylor, M. J.; Jirong, W.; Rickard, C. E. F. Preparation and crystal structure of $MoO_2Cl_2(H_2O)_2 \cdot H_2O \cdot Et_4NCl$ in relation to the nature of the molybdenum(VI) species in hydrochloric acid solutions. *Polyhedron* **1993**, *12* (12), 1433–1435.

(59) Bettinardi, D. J.; Paulenova, A.; Tkac, P. Speciation of molybdenum(VI) in chloride media at elevated Mo concentrations. *ACS Omega* **2020**, *5* (37), 23786–23792.

(60) Zhang, N.; Königsberger, E.; Duan, S.; Lin, K.; Yi, H.; Zeng, D.; Zhao, Z.; Hefter, G. Nature of monomeric molybdenum(VI) cations in acid solutions using theoretical calculations and Raman spectroscopy. *J. Phys. Chem. B* **2019**, *123* (15), 3304–3311.

(61) Oyerinde, O. F.; Weeks, C. L.; Anbar, A. D.; Spiro, T. G. Solution structure of molybdic acid from Raman spectroscopy and DFT analysis. *Inorganica Chim. Acta* **2008**, *361* (4), 1000–1007.

(62) Sergent, N.; Epifani, M.; Pagnier, T. *In situ* Raman spectroscopy study of NO_2 adsorption onto nanocrystalline tin(IV) oxide. *J. Raman Spectrosc*. **2006**, *37* (11), 1272–1277.

(63) Hadjiivanov, K. I. Identification of neutral and charged N_xO_y surface species by IR spectroscopy. *Catal. Rev.* **2000**, *42* (1–2), 71–144.

(64) Nakamoto, K. "Infrared and Raman spectra of inorganic and coordination compounds", in: Handbook of Vibrational Spectroscopy, (John Wiley and Sons, 2006), pp. 1872-1892. DOI: 10.1002/0470027320.s4104

(65) Frost, R. L.; Erickson, K. L.; Kloprogge, T. J. Vibrational spectroscopic study of the nitrate containing hydrotalcite mbobomkulite. *Spectrochim. Acta Mol. Biomol. Spectrosc.* **2005**, *61* (13–14), 2919–2925.

(66) Mousavi, A. How *aqua regia* overcomes the chemical inertness of cinnabar: A thermodynamic analysis in light of long-term knowledge about a reaction that has been of interest for centuries. *Rev. Inorg. Chem.* **2019**, *39* (4), 223–231.

(67) Kozin, A. O.; Zaporozhtseva, Z. G.; Proyavkin, A. A.; Dement'ev, A. A.; Kondrat'ev, Y. V.; Korol'kov, D. V. Enthalpies of reactions of binuclear molybdenum(III), (V), and (VI) ethylenediaminetetracetate, oxo, and hydroxo complexes in aqueous solutions. *Russ. J. Gen. Chem.* **2004**, *74* (5), 687–693.

(68) Ojo, J.; Ipinmoroti, K. O.; Adeeyinwo, C. E. Solvent extraction of molybdenum (VI) from diluted and concentrated hydrochloric acid. *Global J. Pure Appl. Sci*. **2008**, *14* (3), 289–294.

(69) Nyasulu, F. W.; Mayer, J. M. Molybdenum oxychlorides I. Electrochemistry of MoO_2Cl_2: Oxidation, dimerization, and electrodeposition at a platinum electrode. *J. Electroanal. Chem*. **1995**, *392* (1–2), 35–42.

(70) Kumar, V.; Wang, X.; Lee, P. S. Synthesis of pyramidal and prismatic hexagonal MoO_3 nanorods using thiourea. *CrystEngComm*. **2013**, *15* (38), 7663–7669.

(71) Moura, J. V. B.; Silveira, J. V.; da Silva Filho, J. G.; Souza Filho, A. G.; Luz-Lima, C.; Freire, P. T. C. Temperature-induced phase transition in h-MoO_3: Stability loss mechanism uncovered by Raman spectroscopy and DFT calculations. *Vib. Spectros.* **2018**, 98, 98–104.

(72) Maczka, M.; Paraguassu, W.; Souza Filho, A. G.; Freire, P. T. C.; Mendes Filho, J.; Melo, F. E. A.; Hanuza, J. High-pressure Raman study of $Al_2(WO_4)_3$. *J. Solid State Chem.* **2004**, *177* (6), 2002–2006.

(73) Dieterle, M.; Weinberg, G.; Mestl, G. Raman spectroscopy of molybdenum oxides. Part I. Structural characterization of oxygen defects in MoO_{3-x} by DR UV/VIS, Raman spectroscopy and X-ray diffraction. *Phys. Chem. Chem. Phys*. **2002**, *4* (5), 812–821.

(74) Camacho-López, M. A.; Haro-Poniatowski, E.; Lartundo-Rojas, L.; Livage, J.; Julien, C. M. Amorphous-crystalline transition studied in hydrated MoO_3. *Mater. Sci. Eng. B* **2006**, *135* (2), 88–94.

(75) Haro-Poniatowski, E.; Jouanne, M.; Morhange, J. F.; Julien, C.; Diamant, R.; Fernández-Guasti, M.; Fuentes, G. A.; Alonso, J. C. Micro-Raman characterization of WO_3 and MoO_3 thin films obtained by pulsed laser irradiation. *Appl. Surf. Sci*. **1998**, *127–129*, 674–678.

(76) Seguin, L.; Figlarz, M.; Cavagnat, R.; Lassègues, J. -C. Infrared and Raman spectra of MoO_3 molybdenum trioxides and $MoO_3 \cdot xH_2O$ molybdenum trioxide hydrates. *Spectrochim. Acta Part A Mol. Biomol. Spectrosc*. **1995**, *51* (8), 1323–1344.

(77) Yao, D. D.; Ou, J. Z.; Latham, K.; Zhuiykov, S.; O'Mullane, A. P.; Kalantar-zadeh, K. Electrodeposited α- and β-phase MoO_3 films and investigation of their gasochromic properties. *Cryst. Growth Des*. **2012**, *12* (4), 1865–1870.

(78) Camacho-López, M. A.; Escobar-Alarcón, L.; Picquart, M.; Arroyo, R.; Córdoba, G.; Haro-Poniatowski, E. Micro-Raman study of the *m*-MoO_2 to α-MoO_3 transformation induced by cw-laser irradiation. *Opt. Mater. (Amsterdam, Neth.)* **2011**, *33* (3), 480–484

(79) Wang, L.; Li, M. -C.; Zhang, G. -H.; Xue, Z. -L. Morphology evolution and quantitative analysis of β-MoO_3 and α-MoO_3. *High Temp. Mater. Processes (Berlin, Ger.)* **2020**, *39* (1), 620–626.

(80) Ren, T.; Tran, R.; Lee, S.; Bandera, A.; Herrera, M.; Li, X. -G.; Ong, S. P., Graeve, O. A. Morphology control of tantalum carbide nanoparticles through dopant additions. *J. Phys. Chem. C* **2021**, *125* (19), 10665–10675.

(81) Cahill, J. T.; Graeve, O. A. Hexaborides: A review of structure, synthesis and processing. *J. Mater. Res. Technol.* **2019**, *8* (6), 6321–6335.

(82) Qiao, S.; Novitskaya, E.; Ren, T.; Pena, G.; Graeve, O. A. Phase and morphology control of magnesium nanoparticles via lithium doping. *Cryst. Growth Des.* **2019**, *19* (7), 3626–3632.

(83) Frank, M. B.; Siu, S. H.; Karandikar, K.; Liu, C. -H.; Naleway, S. E.; Porter, M. M.; Graeve, O. A.; McKittrick, J. Synergistic structures from magnetic freeze casting with surface magnetized alumina particles and platelets. *J. Mech. Behav. Biomed. Mater.* **2017**, *76*, 153–163.

(84) Kanakala, R.; Escudero, R.; Rojas-George, G.; Ramisetty, M.; Graeve, O. A. Mechanisms of combustion synthesis and magnetic response of high-surface area hexaboride compounds. *ACS Appl. Mater. Interfaces* **2011**, *3* (4), 1093–1100.

(85) Kanakala, K.; Rojas-George, G.; Graeve, O. A. Unique preparation of hexaboride nanocubes: A first example of boride formation by combustion synthesis. *J. Am. Ceram. Soc.* **2010**, *93* (10), 3136–3141.

(86) Atuchin, V. V.; Gavrilova, T. A.; Grigorieva, T. I.; Kuratieva, N. V.; Okotrub, K. A.; Pervukhina, N. V.; Surovtsev, N. V. Sublimation growth and vibrational microspectrometry of α-MoO_3 single crystals. *J. Cryst. Growth* **2011**, *318* (1), 987–990.

(87) Mizushima, T.; Moriya, Y.; Phuc, N. H. H.; Ohkita, H.; Kakuta, N. Soft chemical transformation of α-MoO_3 to β-MoO_3 as a catalyst for vapor-phase oxidation of methanol. *Catal. Commun*. **2011**, *13* (1), 10–13.

(88) Wang, B. G.; Shi, E. W.; Zhong, W. Z. Twinning morphologies and mechanisms of ZnO crystallites under hydrothermal conditions. *Cryst. Res. Technol*. **1998**, *33* (6), 937–941.

(89) Li, Z.; Ma, J.; Zhang, B.; Song, C.; Wang, D. Crystal phase- and morphology-controlled synthesis of MoO_3 materials. *CrystEngComm* **2017**, *19* (11), 1479–1485.

(90) Torres, D.; Jiang, Y.; Sanchez-Monsalve, D. A.; Leeke, G. A. Hydrochloric acid removal from the thermogravimetric pyrolysis of PVC. *J. Anal. Appl. Pyrolysis* **2020**, *149*, 104831.

Figure Captions

Figure 1. (a) Calculated Raman spectrum of $[MoO_2Cl_3(H_2O)]^-$ and recorded Raman spectra of solutions (b) A0, (c) A5, (d) A10, and (e) A15. The Raman spectra is illustrated from 200 to 450 cm^{-1} and from 800 to 1100 cm^{-1}.

Figure 2. (a) Raman shift of the symmetric stretching vibration of Mo=O *vs* NaCl added to solutions A0 to A15. The horizontal dashed lines at 963 and 943 cm^{-1} show the calculated Raman shift for the symmetric stretching vibration of Mo=O in $[MoO_2Cl_3(H_2O)]^-$ and $[MoO_2Cl_4]^{2-}$, respectively. (b) Raman shift of the symmetric stretching vibration of N-O *vs* NaCl added to solutions A0 to A15. The horizontal dashed lines show the reported Raman shift for the symmetric vibration of N-O at 1050 cm^{-1} for HNO_3 and at 1045 cm^{-1} for NO_3^-.[65]

Figure 3. X-ray diffraction patterns of powders obtained after thermal treatment of solutions (a) A0, (b) A5, (c) A10, and (d) A15. Polyhedral representations of (e) α–MoO_3, (f) β–MoO_3 and (g) *h*–MoO_3. The letter A in (g) represents the sites where ammonia or water molecules are contained to stabilize the hexagonal phase of MoO_3.

Figure 4. Raman spectra of samples (a) AP0, (b) AP5, (c) AP10, and (d) AP15. Numbers 1 to 12 indicate the Raman vibrations. The numbers with an α superscript indicate Raman vibrations belonging to α–MoO_3. The numbers with a β*h* superscript indicate Raman vibrations reported for β–MoO_3 and *h*–MoO_3, and the rest of the numbers indicate Raman vibrations assigned to *h*–MoO_3 only.

Figure 5. Scanning electron micrographs of (a)-(d) AP0, (e)-(h) AP5, (i)-(l) AP10, and (m)-(p) AP15. The rectangles in (k) and (p) indicate the regions from which energy dispersive spectra were obtained (spectra shown in Figure 6).

Figure 6. Energy dispersive spectra from the darker regions in sample AP10 and AP15, illustrated with rectangles in Figures 5(k) and (p), respectively.

Figure 7. Proposed scheme for the synthesis of *h*–MoO_3, α–MoO_3, and β–MoO_3.

Figure 8. Calorimetry curves of samples (a) AP0 and (b) AP5.

Figure 9. Calorimetry curves of samples (a) AP10 and (b) AP15.

Tables

Table 1. Calculated Raman peaks of $MoO_2Cl_2(H_2O)_2$, $[MoO_2Cl_4]^{2-}$, $[MoO_2Cl_3(H_2O)]^-$, and recorded Raman bands from solutions A0, A5, A10, and A15.

	Vibration assignment	Calculated Raman vibrations (cm^{-1})				Recorded Raman vibrations (cm^{-1})			
Vibration number		$MoO_2Cl_2(H_2O)_2$	$[MoO_2Cl_4]^{2-}$	$[MoO_2Cl_3(H_2O)]^-$	Band assignment	A0	A5	A10	A15
1	w(Mo-O)	216	-	220	I	244 ± 1	247 ± 0	241 ± 3	240 ± 3
2	r(O-Mo-O)	226	-	225					
3	t(O-Mo-O)	249	-	261					
4	ν_s(Mo-Cl)	269	275	295	II	305 ± 4	305 ± 12	295 ± 6	289 ± 5
5	ν(Mo-OH_2)	346	-	309					
6	δ(O-Mo-O)	388	355	357	III	385 ± 10	377 ± 1	369 ± 2	370 ± 3
7*	ν_{asym}(Mo=O)	933	912	920	IV*	924 ± 0	917 ± 3	927 ± 2	919 ± 6
8*	ν_{sym}(Mo=O)	973	943	963	V*	962 ± 1	960 ± 1	957 ± 2	956 ± 2
-	–	-	-	-	VI**	1052 ± 1	1051 ± 1	1048 ± 2	1047 ± 2

* Most intense Raman peaks in the region from 200-1100 cm^{-1}.

** Raman vibration only observed in the experimental Raman spectra corresponding to the ν_{sym}(N-O) vibration from the HNO_3 used during synthesis.

Table 2. Raman vibrations previously reported for *h*–MoO_3. The Raman vibrations include twisting (tw), scissoring (sc), rotational (ρ), symmetric stretching (ν_s), and asymmetric stretching (ν_a).

Lunk *et al.*[12] (cm^{-1})	Pan *et al.*[20] (cm^{-1})	Silveira *et al.*[37] (cm^{-1})	Atuchin *et al.*[38] (cm^{-1})	Moura *et al.*[71] (cm^{-1})		Assignment, Moura *et al.*[71] (cm^{-1})
				Calculated	Experimental	
222	217	220	219	215	217	tw(MoO_2) (c-axis)
				233		sc(MoO_2) (a-b plane)
253	250	249	250	243	247	tw(MoO_2) (c-axis)
316	312	318	319	304	315	tw(MoO_2) (a-b plane)
				314		tw(MoO_2) (a-b plane)
396		397	398	381	397	sc(MoO_2) (a-b plane)
414	412	415		385	414	sc(MoO_2) (a-b plane)
				482		ρ(MoO_2) (a-b plane)
492	489	493	492	488	490	ρ(MoO_2) (a-b plane)
690	690	695	691	702	690	sc(MoO_2) (c-axis)
	887	885	880	843	878	ν_a(MoO_2) (a-b plane)
900	901	903	901	882	900	ν_a(MoO_2) (a-b plane)
	916	923	912		915	-
973	980	982	978	952	977	ν_s(MoO_2) (a-b plane)
				953	988	ν_s(MoO_2) (a-b plane)

Table 3. Raman vibrations of samples AP0 to AP15. The Raman vibration assignment is based on a previous report by Moura *et al*.[71] on hexagonal MoO_3. The Raman vibrations include twisting (tw), scissoring (sc), rotational (ρ), bending (δ), symmetric stretching (ν_s), and asymmetric stretching (ν_a).

Raman vibration	Assignment	Raman mode	AP0 (cm^{-1})	AP5 (cm^{-1})	AP10 (cm^{-1})	AP15 (cm^{-1})
1	sc(O-Mo-O) (a-b plane)	A_g	230	231		
2	tw(O-Mo-O) (c-axis)	E_{1g}		257	255	253
3	sc(O-Mo-O) in α–MoO_3	-	264			
4	δ(O-Mo-O) in α–MoO_3		283	280		276
5	tw(O-Mo-O) (a-b plane)	E_{2g}			321	
6	sc(O-Mo-O) (a-b plane)	E_{2g}	401	399	402	395
7	sc(O-Mo-O) (a-b plane)	A_{gh}	$416^{\beta,h}$	$415^{\beta,h}$	$417^{\beta,h}$	$413^{\beta,h}$
8	ν(Mo-O) in α–MoO_3		476			476
9	ρ(O-Mo-O) a-b plane	A_g	497	497	495	491
10	sc(O-Mo-O) (c axis)	E_{1g}	680	679		675
11	sc(O-Mo-O) (c axis)	E_{1g}	705	699	695	697
12	ν(Mo=O) in α–MoO_3		829	825	836	
13	ν_a(Mo=O) (a-b plane)	E_{2g}		882	880	882
14	ν_a(Mo=O) (a-b plane)	E_{2g}		$903^{\beta,h}$	$903^{\beta,h}$	
15	-	-	916	913	917	910
16	-	-				924
17	-	-	932			
18	ν_s(Mo=O) (a-b plane)	E_{2g}	988	986	983	981
19	ν_s(Mo=O) (a-b plane)	E_{2g}	993	990		987

$^{\beta,h}$ Vibration observed in β–MoO_3 and *h*–MoO_3 crystals.

Table 4. Summary of the DSC/DTG temperatures and weight loss percentages according to thermogravimetric analysis for the powders.

Reaction	Temperature from DSC (K)				Temperature from DTG (K)				Weight loss (%) from TGA			
	AP0	AP5	AP10	AP15	AP0	AP5	AP10	AP15	AP0	AP5	AP10	AP15
Elimination of surface-adsorbed water	-	-	-	-	-	398	393	393	6	6.5	5.2	6.1
Elimination of surface-adsorbed nitrate compounds	503	498	502	505	503	488	494	493				
Elimination of surface-adsorbed HCl	557	543	545	548	550	536	531	541				
Dehydration from the internal crystal structure	-	-	-	-	-	643	646	647				
Phase transformation from β–MoO_3 to α–MoO_3	663	619	-	-	-	-	-	-				
Phase transformation from *h*–MoO_3 to α–MoO_3	706	648	649	650	-	-	-	-				

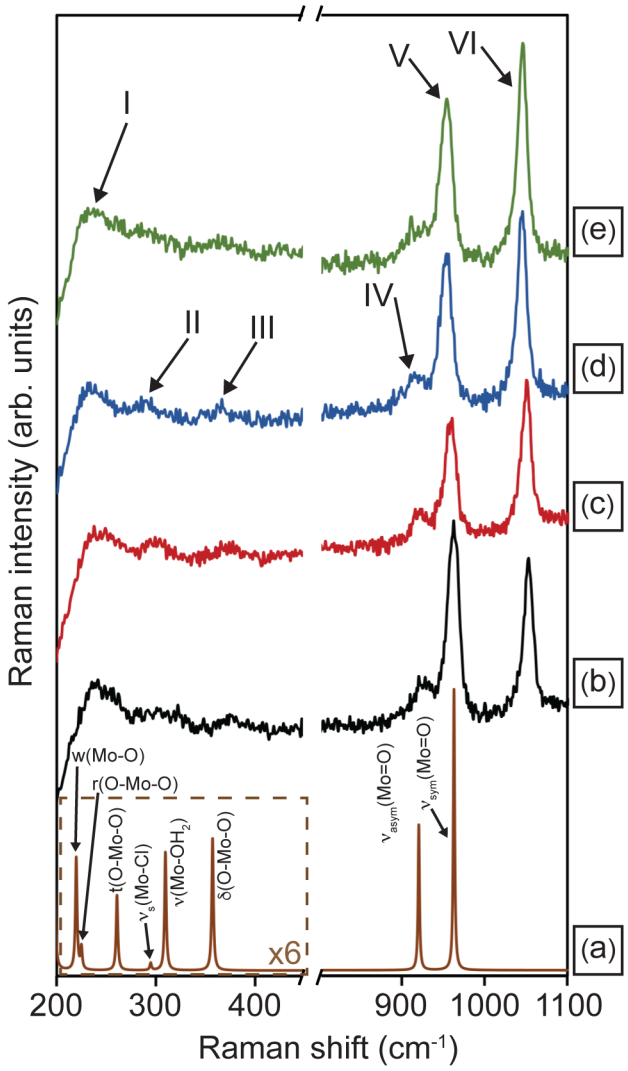

Figure 1. (a) Calculated Raman spectrum of $[MoO_2Cl_3(H_2O)]^-$ and recorded Raman spectra of solutions (b) A0, (c) A5, (d) A10, and (e) A15. The Raman spectra is illustrated from 200 to 450 cm^{-1} and from 800 to 1100 cm^{-1}.

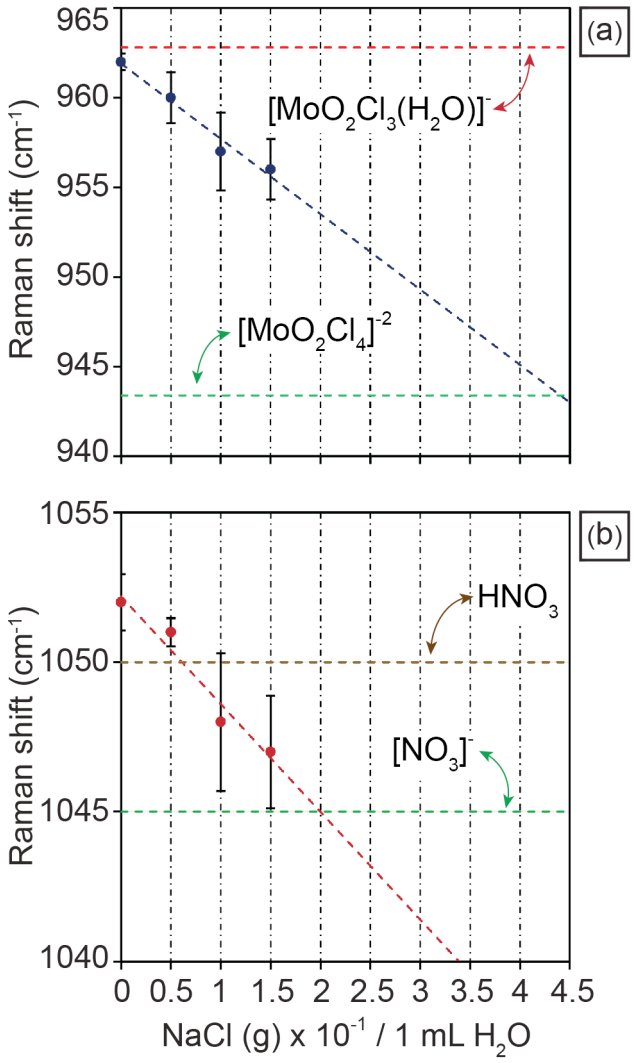

Figure 2. (a) Raman shift of the symmetric stretching vibration of Mo=O *vs* NaCl added to solutions A0 to A15. The horizontal dashed lines at 963 and 943 cm^{-1} show the calculated Raman shift for the symmetric stretching vibration of Mo=O in $[MoO_2Cl_3(H_2O)]^-$ and $[MoO_2Cl_4]^{2-}$, respectively. (b) Raman shift of the symmetric stretching vibration of N-O *vs* NaCl added to solutions A0 to A15. The horizontal dashed lines show the reported Raman shift for the symmetric vibration of N-O at 1050 cm^{-1} for HNO_3 and at 1045 cm^{-1} for NO_3^-.[65]

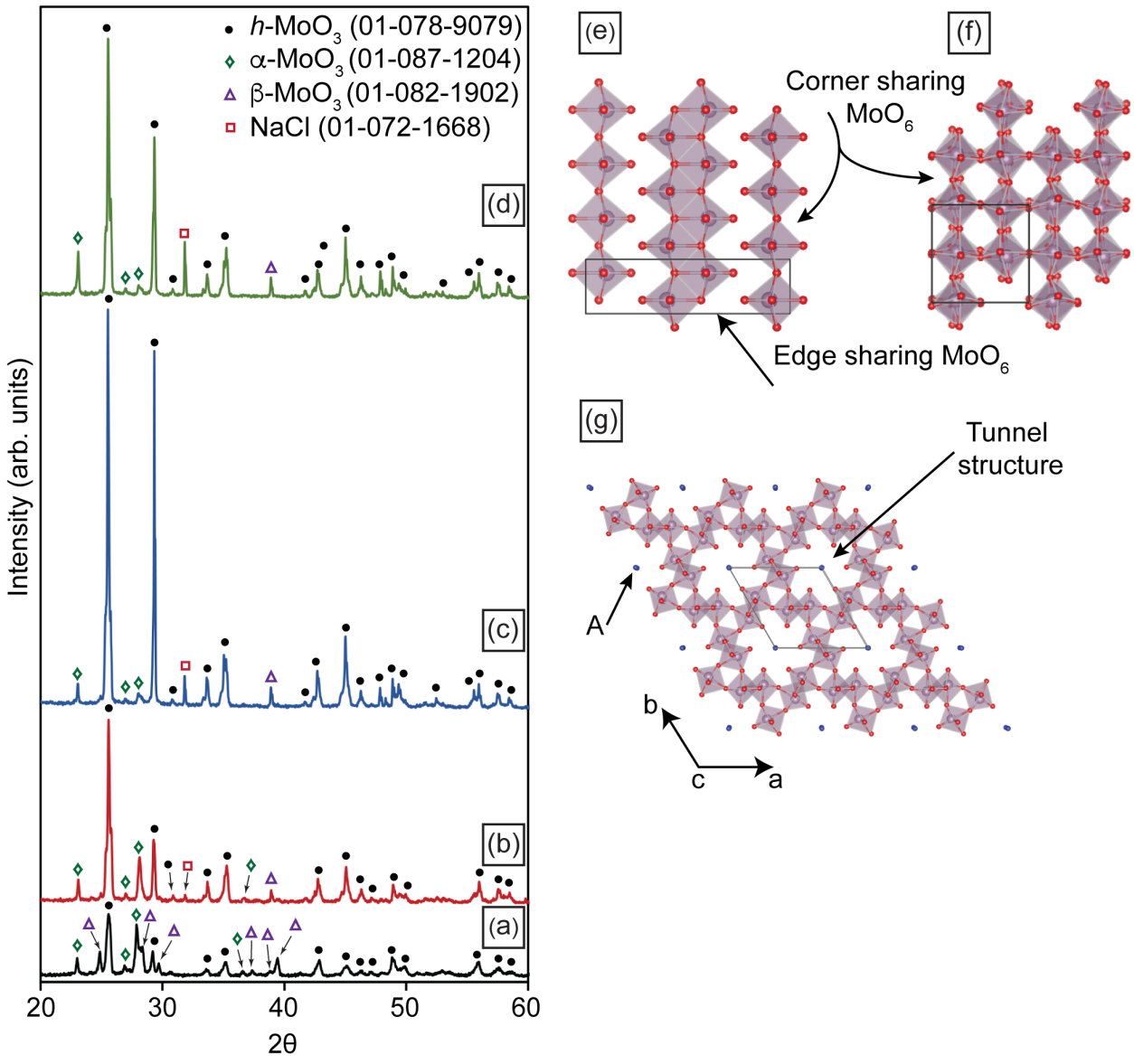

Figure 3. X-ray diffraction patterns of powders obtained after thermal treatment of solutions (a) A0, (b) A5, (c) A10, and (d) A15. Polyhedral representations of (e) α–MoO_3, (f) β–MoO_3 and (g) *h*–MoO_3. The letter A in (g) represents the sites where ammonia or water molecules are contained to stabilize the hexagonal phase of MoO_3.

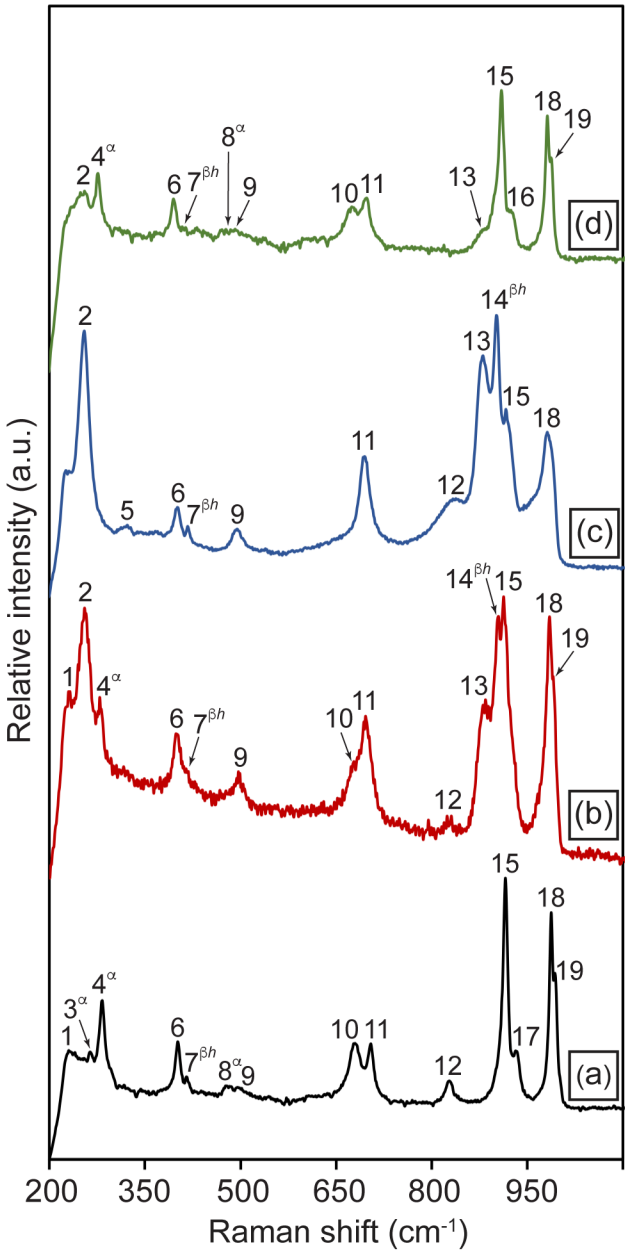

Figure 4. Raman spectra of samples (a) AP0, (b) AP5, (c) AP10, and (d) AP15. Numbers 1 to 12 indicate the Raman vibrations. The numbers with an α superscript indicate Raman vibrations belonging to α–MoO_3. The numbers with a β*h* superscript indicate Raman vibrations reported for β–MoO_3 and *h*–MoO_3, and the rest of the numbers indicate Raman vibrations assigned to *h*–MoO_3 only.

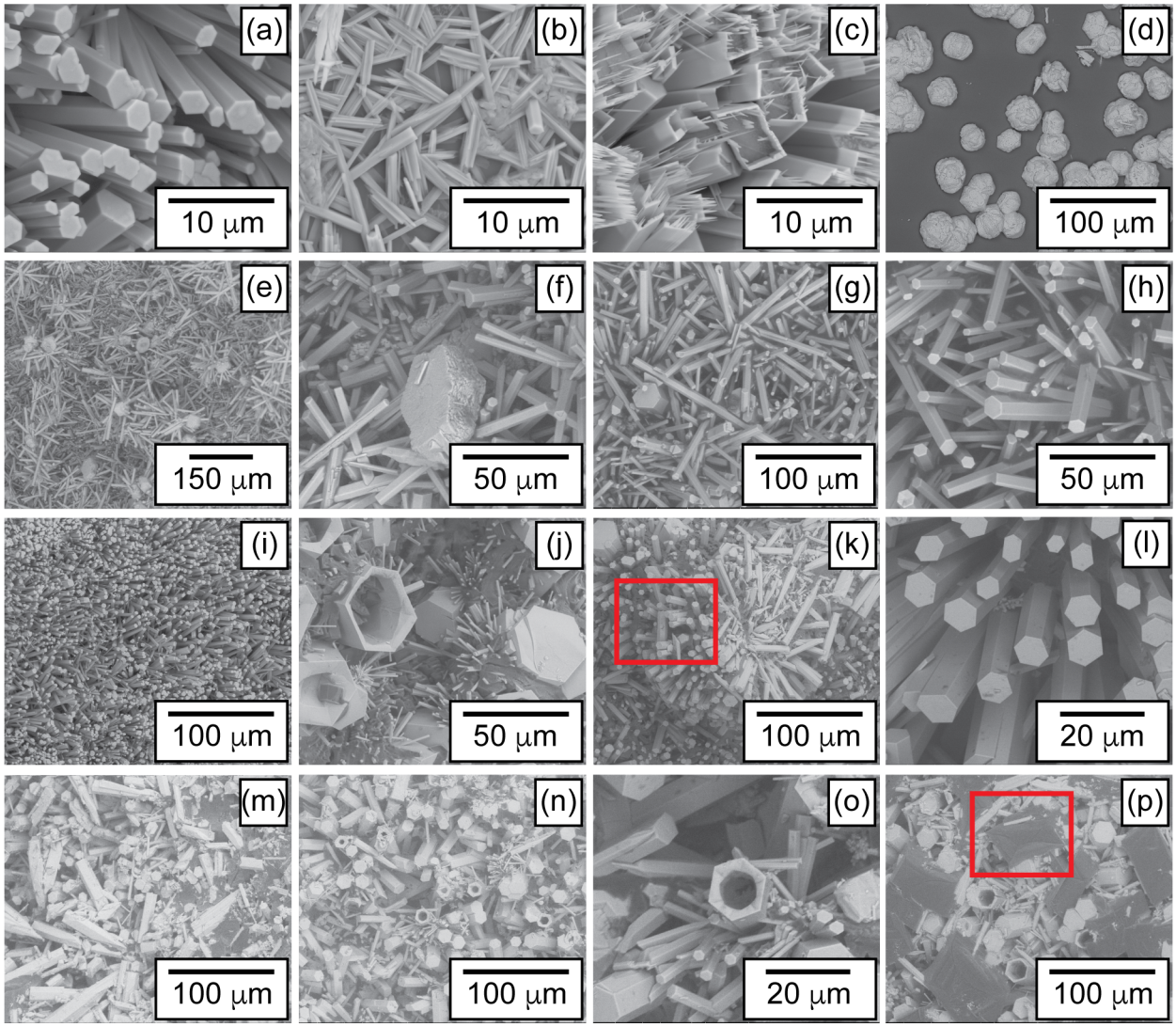

Figure 5. Scanning electron micrographs of (a)-(d) AP0, (e)-(h) AP5, (i)-(l) AP10, and (m)-(p) AP15. The rectangles in (k) and (p) indicate the regions from which energy dispersive spectra were obtained (spectra shown in Figure 6).

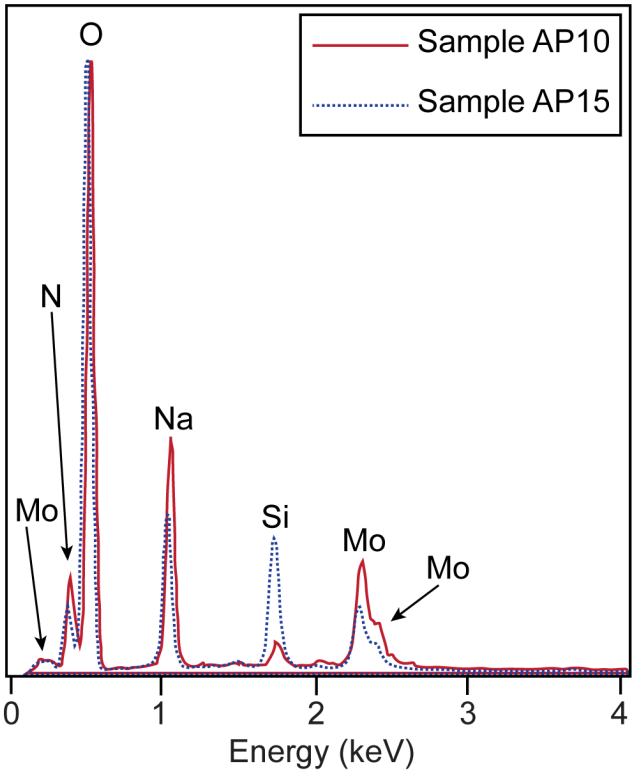

Figure 6. Energy dispersive spectra from the darker regions in sample AP10 and AP15, illustrated with rectangles in Figures 5(k) and (p), respectively.

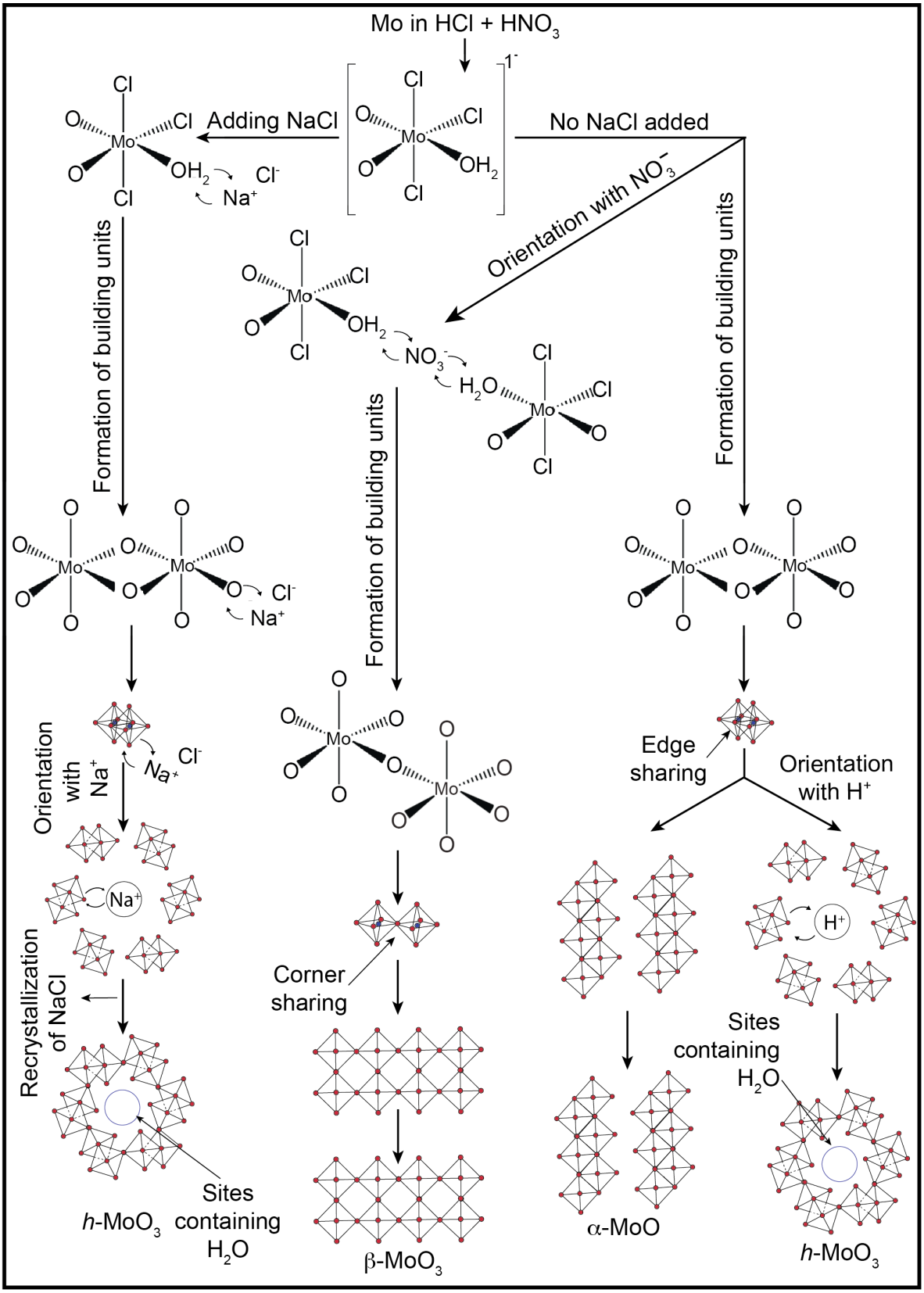

Figure 7. Proposed scheme for the synthesis of *h*–MoO_3, α–MoO_3, and β–MoO_3.

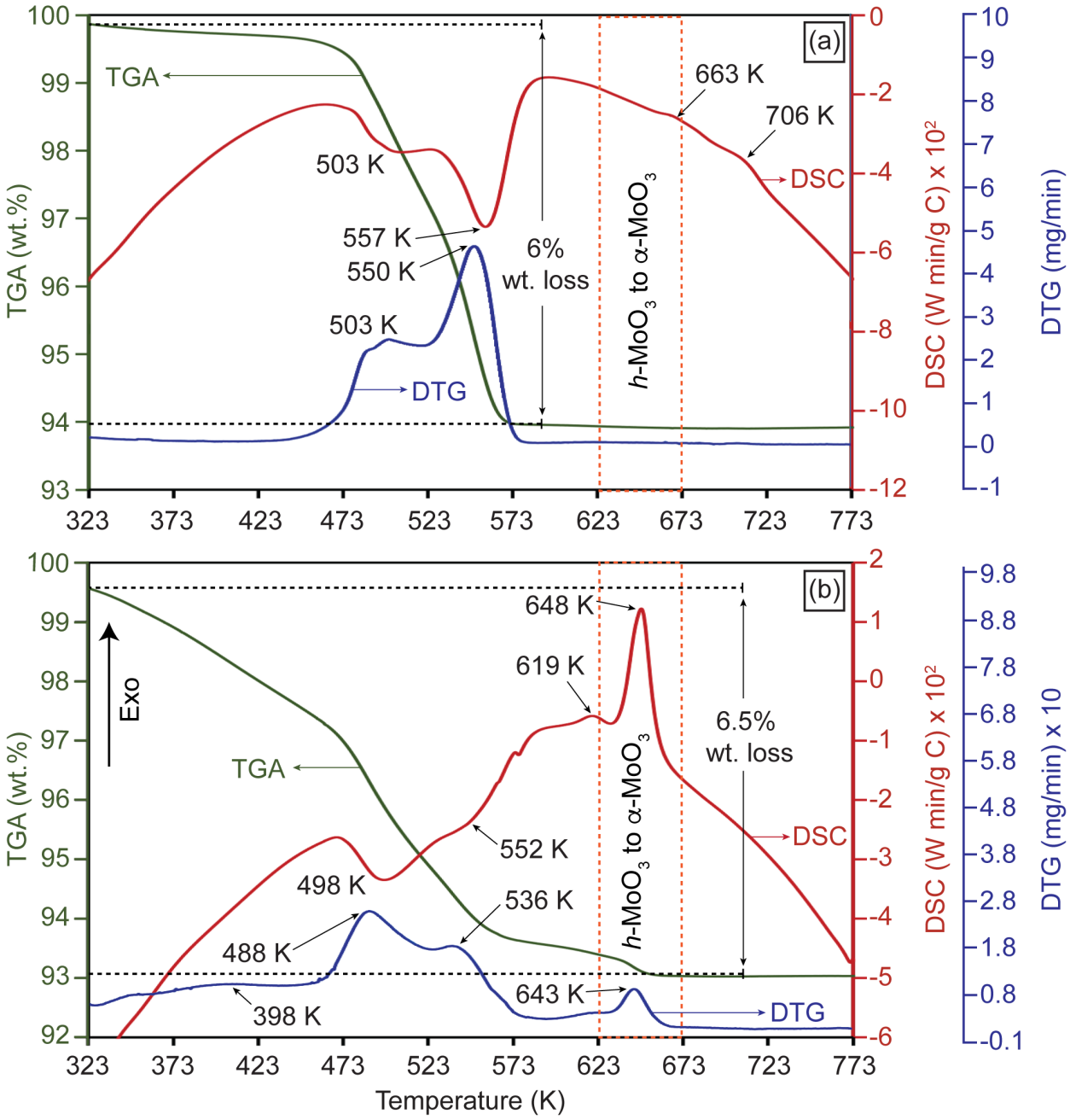

Figure 8. Calorimetry curves of samples (a) AP0 and (b) AP5.

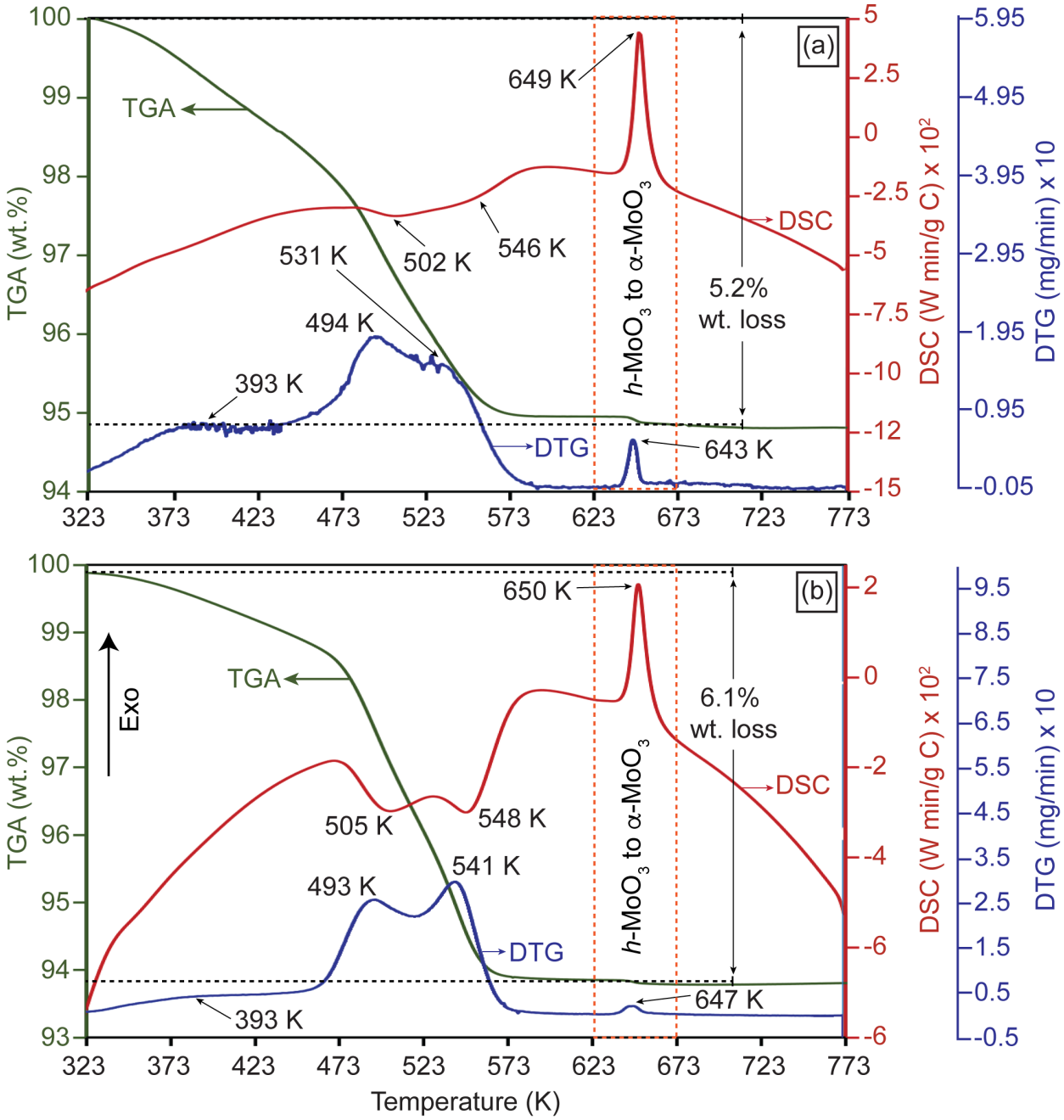

Figure 9. Calorimetry curves of samples (a) AP10 and (b) AP15.

Table of Contents Graphic